Atmos. Chem. Phys., 26, 16341–16372, 2026
https://doi.org/10.5194/acp-26-16341-2026
© Author(s) 2026. This work is distributed under
the Creative Commons Attribution 4.0 License.

Atmospheric Chemistry and Physics
Open Access
EGU

Airborne and marine microplastics in the Northern Indian Ocean: decoupled pathways traced by black carbon

Piotr Markuszewski[1,2,3,4], Mikołaj Mazurkiewicz[1], Kinga Stawiarz[5], Małgorzata Śmiszek[5], Patrycja Jutrzenka-Trzebiatowska[6], Luca Ferrero[3], Krishnakant Budhavant[7,8], Mateusz Zawadzki[5], Anna Waleczek[9], Przemysław Makuch[1], Douglas Nilsson[2,4], Örjan Gustafsson[2,4], and Sophie L. Haslett[2,4]

[1]Institute of Oceanology, Polish Academy of Sciences, 81-712, Sopot, Poland
[2]Department of Environmental Science, Stockholm University, 10691, Stockholm, Sweden
[3]GEMMA and POLARIS Centre, Università degli Studi di Milano-Bicocca, Milano, Italy
[4]Bolin Centre for Climate Research, Stockholm University, 10691, Stockholm, Sweden
[5]Division of Electron Collisions Physics, Institute of Physics and Applied Computer Science, Faculty of Applied Physics and Mathematics, Gdańsk University of Technology, ul. G. Narutowicza 11/12, Gdańsk, 80-233, Poland
[6]Department of Environmental Technology, Faculty of Chemistry, University of Gdańsk, 80-308 Gdańsk, Poland
[7]Maldives Climate Observatory-Hanimaadhoo (MCOH), Maldives Meteorological Services, H. Dh. Hanimaadhoo 02020, Maldives
[8]Divecha Centre for Climate Change, Indian Institute of Science, Bangalore 560012, India
[9]Faculty of Oceanography and Geography, University of Gdańsk, al. J. Piłsudskiego 46, Gdynia, 81–378, Poland

Correspondence: Piotr Markuszewski (pmarkusz@iopan.pl)

Received: 27 July 2026 – Discussion started: 27 August 2026
Revised: 3 November 2026 – Accepted: 4 November 2026 – Published: 17 November 2026

Abstract. Microplastics (MPs) have been detected in both marine and atmospheric particulate matter, but their sources, transport, and air–sea exchange remain poorly constrained in remote marine regions. We investigated airborne microplastics (AMPs) and marine microplastics (MMPs) during a 1-month campaign at the Maldives Climate Observatory Hanimaadhoo and in adjacent coastal waters. Airborne particles were collected with a deposition box, and seawater was sampled at coastal sites. Particle morphology, size, and polymer composition were determined by optical microscopy and μ-Raman spectroscopy and evaluated alongside aerosol scattering and equivalent black carbon (eBC). AMP concentrations ranged from 0 to 10.3 MP m^{-3} (mean: 3.1 ± 2.8 MP m^{-3}). MMP concentrations ranged from 120 to 2656 MP m^{-3} (mean: 876 ± 804 MP m^{-3}), exceeding typical open-ocean values and indicating substantial local influence from inhabited islands and maritime activity. Significant differences in size distributions and pronounced compositional differences of AMPs and MMPs suggest weak coupling between the atmospheric and marine reservoirs. Low dry-season wind speeds probably suppressed wave breaking, bubble bursting, and sea-spray-mediated transfer from ocean to atmosphere. Instead, AMP variability coincided with polluted air-mass advection, elevated eBC, and enhanced aerosol scattering, indicating stronger control by regional atmospheric transport than by local marine emissions. These results show that remote island atmospheres are exposed to anthropogenic plastic aerosol transport and demonstrate the value of combining MP observations with established aerosol tracers to resolve plastic-particle pathways in marine environments.

Published by Copernicus Publications on behalf of the European Geosciences Union.

1 Introduction

Microplastic (MP) contamination is now recognised as a widespread environmental problem affecting both the ocean and the atmosphere (Allen et al., 2022). The marine environment is considered a major reservoir of MPs. Still, these particles are also increasingly detected in air, where they behave as aerosol particles, can be transported over long distances, and may later be deposited back to the sea surface or land (Allen et al., 2019; Ferrero et al., 2022). This implies active exchange between the ocean and atmosphere and highlights the need to study both compartments together. Such interactions may be especially important in island regions of the Indian Ocean, where MP levels can be influenced by both local human activity and regional transport from densely populated and industrialised areas (Pattiaratchi et al., 2022).

MPs are typically defined as plastic particles smaller than 5 mm. They are commonly divided into primary and secondary forms. Primary MPs are manufactured directly as small pellets or fibres, whereas secondary MPs originate from the degradation of larger plastic items through physical, chemical, or biological processes (Boucher and Friot, 2017). In the marine environment, MPs can affect a wide range of organisms and destabilise ecosystems, and global marine MP concentrations have increased substantially over recent decades (Auta et al., 2017). At the same time, airborne microplastics (AMPs) are emerging as an important concern in South Asia, where they are increasingly considered part of regional aerosol chemistry, raising questions about their sources, transport pathways, deposition, and long-term environmental and human health effects (Perera et al., 2022; Kannankai and Devipriya, 2024).

The Maldives is a particularly relevant setting in which to investigate these processes. The country consists of low-lying coral islands and is highly vulnerable to MP pollution because of its geographic exposure and limited waste-management capacity. Marine microplastics (MMPs) have already been documented across several Maldivian islands and atolls, including Vavvaru (Imhof et al., 2017), Naifaru (Patti et al., 2020), Faafu Atoll (Saliu et al., 2018), and Magoodhoo (Raguso et al., 2022). These studies point to a complex and interconnected pollution landscape, in which polymers such as polyethylene (PE) and polypropylene (PP) recur and may indicate shared source types and degradation pathways (Wang et al., 2020; Trainic et al., 2020). The ecological implications are substantial. MPs have been detected in reef-building corals, emphasising the vulnerability of one of the most biodiverse and sensitive ecosystems in the Indian Ocean, and reported impacts include tissue abrasion and the possible leaching of additives (Raguso et al., 2022; Isa et al., 2025). In contrast, much less attention has been paid to the role of airborne transport in redistributing plastic particles and influencing environmental concentrations, including those in the marine environment.

The regional anthropogenic context is equally important. In 2019, the Republic of Maldives was ranked as the fourth-largest per-capita waste producer globally (Stevens and Froman, 2019). This ranking is largely linked to rapid tourism growth and increasing urban waste generation (Rifa and Hossain, 2022). During the last decade, per-capita waste production increased by about 58 %, placing strong pressure on national waste-management infrastructure. A key symbol of this problem is Thilafushi, a lagoon converted into a landfill island in 1992, which now receives around 700 t of waste daily from nearby islands (Kapmeier and Gonçalves, 2018; Kaza et al., 2018; Munshi et al., 2022). Open-air burning and unregulated landfilling at Thilafushi are likely important regional sources of incomplete combustion products, including black carbon and potentially AMPs (Dasari et al., 2025). The open burning of mixed waste releases a complex mixture of pollutants, including fine and coarse particulate matter ($PM_{2.5}$ and PM_{10}), which may contain AMPs and black carbon, together with toxic gases and semi-volatile organic compounds such as carbon monoxide, volatile organic compounds, and polycyclic aromatic hydrocarbons (Budhavant et al., 2015; Kováts et al., 2022; Islam et al., 2022).

In the Maldives, the interaction between airborne and oceanic plastic pollution is of particular concern because of the country's geographic setting and strong dependence on marine resources (Royle et al., 2022). Air–sea exchange processes, including sea spray and windborne transport, are thought to facilitate the transfer of MPs between the ocean and atmosphere, even in remote environments (Ferrero et al., 2022). Deposition of AMPs into marine systems may increase toxicity in marine ecosystems (Ferrero et al., 2022), while the release of MMPs into the atmosphere through bubble-bursting processes may degrade air quality and increase risks to human health (Oehlschlägel et al., 2024). These source–sink relationships must therefore be constrained to understand how exchange processes influence both AMP and MMP populations.

Airborne transport is also directly relevant for human exposure. Particle size, aerodynamic diameter and shape influence penetration and deposition within the respiratory tract (Donaldson and Tran, 2002; Vasse and Melgert, 2024). Polymers such as PP, PE, and polyterephthalate (PET) have been reported among the predominant types detected in peripheral lung tissue (Donaldson and Tran, 2002; Vasse and Melgert, 2024).

AMPs also need to be considered within the broader atmospheric aerosol framework. Atmospheric aerosols in general, and absorbing aerosols in particular, play a key role in regional air quality and climate. In the Maldivian context, black carbon is especially relevant because it is emitted by incomplete combustion associated with open waste burning, diesel transport, biomass combustion, and residential energy use, all of which are plausible in island settings with limited waste-management capacity (Gustafsson et al., 2026; Bond et al., 2013; Ramanathan and Carmichael, 2008). In tropical

and marine boundary layers, black carbon affects radiative balance, boundary-layer stability, and cloud microphysical processes, while also acting as an effective tracer of local and regional anthropogenic influence (Nair et al., 2023; Andreae and Rosenfeld, 2008; Ramanathan et al., 2001).

Airborne fibres, including microplastics, have been documented in indoor and outdoor environments (Dris et al., 2017), while atmospheric transport and ocean–atmosphere exchange are recognised components of the plastic cycle (Brahney et al., 2021; Allen et al., 2022). Joint observations of AMPs and aerosol optical properties provide an opportunity to examine how AMP abundance varies with atmospheric aerosol conditions. In this study, equivalent black carbon (eBC) is used as a contextual indicator of combustion-derived aerosol influence, while aerosol light scattering provides complementary information on aerosol conditions. Relationships between AMP abundance and these aerosol indicators remain poorly constrained, particularly in remote island regions influenced by both marine aerosol production and combustion-derived particles.

To address these gaps, this study investigates MP contamination in both the atmospheric and marine environments around the Maldives using intensive one-month measurements conducted near the Hanimaadhoo research station. We test whether AMPs in the northern Indian Ocean are primarily linked to local oceanic emissions or to transported anthropogenic aerosol regimes. Specifically, the study aims to (1) quantify MMPs and AMPs and determine their physical properties and polymer composition, (2) assess whether air–sea interaction processes influence MP variability, and (3) assess the co-variability of AMPs with eBC and aerosol light scattering under different advection regimes, using eBC as a contextual indicator of combustion-derived aerosol influence.

2 Measurements

2.1 Sampling site

Atmospheric sampling and the majority of water sampling were carried out at the Maldives Climate Observatory Hanimaadhoo (MCOH, 6.776° N, 73.183° E). The Republic of Maldives is an island nation located in the Indian Ocean. Hanimaadhoo, one of the larger islands, measures approximately 7 km long and 750 m wide. The climate observatory is located at the northern tip of the island. The present study forms part of a broader research project described by Stegelius et al. (2026).

MCOH is a well-established regional receptor site for studying atmospheric outflow from South Asia over the northern Indian Ocean. The site experiences minimal direct local, in-island anthropogenic emissions (Sheesley et al., 2012; Budhavant et al., 2018, 2023), making it particularly suitable for investigating aged aerosol transported from the Indian subcontinent and surrounding source regions, as well as for characterising regional background marine air masses. Previous studies at MCOH have documented strong seasonal contrasts in aerosol chemical composition, optical properties, black carbon, brown carbon, sulfate, and source-diagnostic tracers, reflecting the alternating influence of polluted continental outflow and cleaner marine air masses (Budhavant et al., 2018, 2020, 2023, 2024; Nair et al., 2023; Clarke et al., 2026).

During the winter period, from December to February, northeasterly winds dominate over the region (Ramana and Ramanathan, 2006; Nair et al., 2023; Budhavant et al., 2024). This circulation pattern facilitates the long-range transport of polluted and atmospherically processed air masses from the Indo-Gangetic Plain and other South Asian source regions towards the Maldives, including transport pathways over the Bay of Bengal and the Arabian Sea. The present January–February 2023 campaign was conducted during the established South Asian winter outflow regime, when MCOH is expected to be influenced by transported anthropogenic aerosol mixed with regional marine and island-scale contributions.

This winter regime contrasts with the summer monsoon, when south-westerly winds typically bring cleaner, moist marine air masses from the Southern Indian Ocean (Budhavant et al., 2018, 2020, 2023). This seasonal contrast makes MCOH a valuable receptor site for studying aerosol transport across the northern Indian Ocean. The present study, however, focuses specifically on the January–February winter outflow period.

2.2 Sample collection and laboratory procedures

2.2.1 Airborne sampling

In this study, Total Suspended MicroParticles (TSMP), including AMPs (González-Pleiter et al., 2021), were collected using a custom-built Deposition Box (Ferrero et al., 2018, 2022). This $50 \times 50 \times 20\,cm^3$ box, covered by a pitched roof to minimise environmental interference, integrates passive and active sampling features. Air is drawn at a flow rate of $1.5\,m^3\,h^{-1}$, corresponding to approximately 30 air exchanges per hour. This results in a low internal flow speed ($0.002\,m\,s^{-1}$), below ambient wind speeds. This creates conditions that favour dry deposition without particle stacking, thereby improving individual-particle isolation.

The Deposition Box was mounted on the tower's top at 15 m above ground level. Glass microscope slides ($26 \times 76\,mm^2$) were used as substrates for the collection of TSMP. Prior to deployment, slides were cleaned with purified water and acetone, labelled, then stored in pre-cleaned, sealed aluminium containers. During sampling, they were secured on the stainless-steel grid inside the box and returned to the containers afterwards to minimise contamination.

In total, 48 samples were collected between 13 January–4 February 2023, comprising 46 environmental samples and

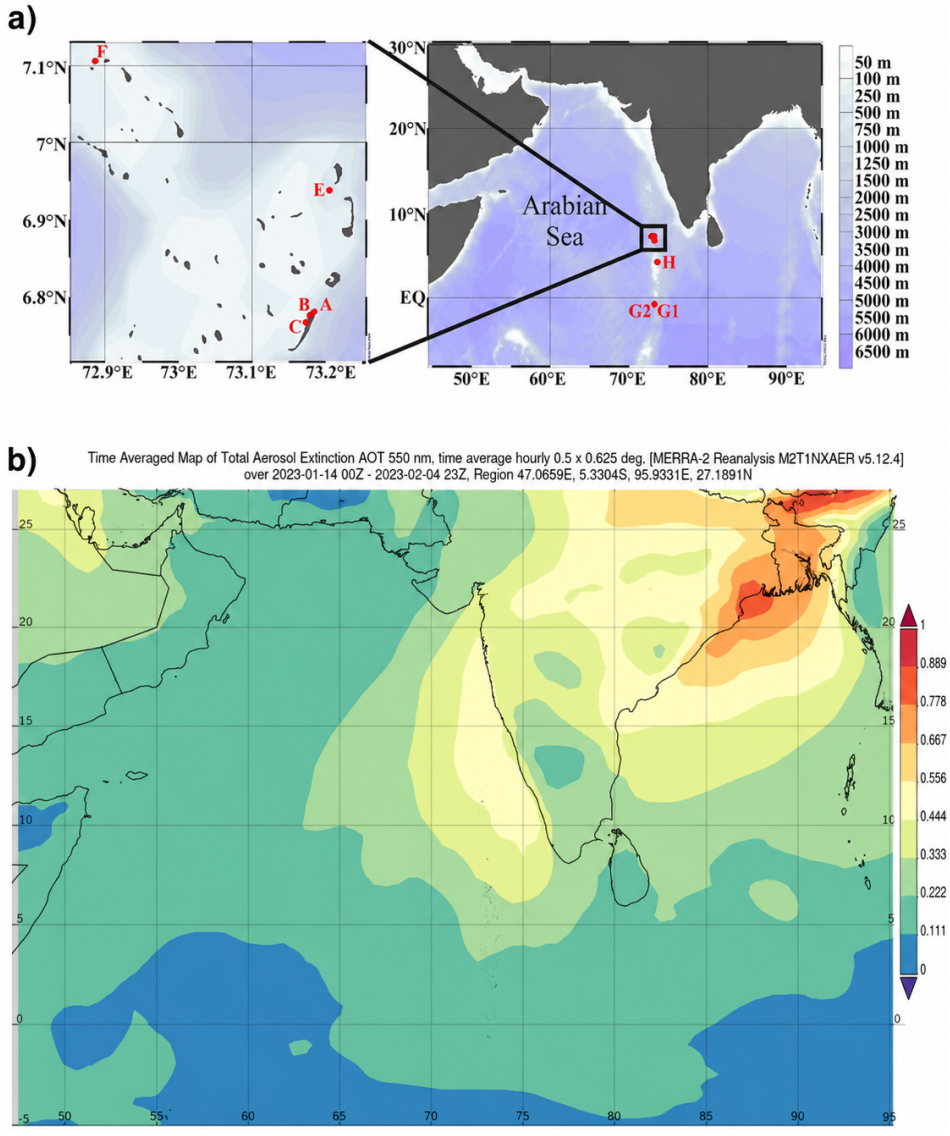

Figure 1. Study area, sampling locations, and regional aerosol conditions during the campaign in the northern Indian Ocean. **(a)** Location of the study area and sampling sites. The regional map shows the Arabian Sea and northern Indian Ocean, with bathymetry indicated by the colour scale in metres. The black box marks the Maldives archipelago. The detailed inset shows Hanimaadhoo Island and nearby islands, with coastal seawater sampling locations marked in red. A–C: Hanimaadhoo Island; E: Kelaa Island; F: Thuraakunu Island; G1–G2: Gan; H: Hulhumalé Island. Airborne microplastic measurements were conducted at the Maldives Climate Observatory Hanimaadhoo (MCOH). The maps were generated using Ocean Data View (ODV; Schlitzer, 2025). **(b)** Time-averaged total aerosol extinction aerosol optical thickness at 550 nm over the northern Indian Ocean for 14 January–4 February 2023, derived from MERRA-2 M2T1NXAER v5.12.4 (Global Modeling and Assimilation Office, 2015) and visualised using Giovanni (Acker and Leptoukh, 2007). The colour scale represents the regional aerosol loading and provides the atmospheric transport context for the microplastic observations.

two laboratory blanks (samples 11 and 12). Exposure durations ranged from approximately 25 to 528 h and were deliberately varied to investigate possible effects of exposure time on microplastic accumulation on the collection slides. Slides were exposed in parallel and retrieved after different intervals, resulting in overlapping sampling periods covering shorter and longer exposures. Individual sampling intervals are listed in Table B2.

The exploratory comparison of concentrations between wind sectors used the short-exposure subset (approximately 25–55 h). Parallel slides with identical sampling intervals were averaged. Where short exposures shared a start time, the longer window was retained to maximise temporal coverage without overlap. This yielded ten non-overlapping sampling windows, with five assigned to each wind sector. Differences were assessed using the two-sided Kolmogorov–

Smirnov statistic, with exact permutation p values calculated from all 252 allocations of sector labels.

For the exploratory aerodynamic-diameter comparison, particle values were first averaged within each slide, and parallel slide means were then averaged within each retained sampling window. Only windows containing particles with assigned material densities were included, yielding four northerly and three easterly windows. Exact permutation p values were calculated using the two-sided Kolmogorov–Smirnov statistic across all 35 allocations of sector labels.

For each sample, exposure duration was incorporated into the concentration calculation through the sampled air volume, determined as $V = Q \times \Delta t$, where Q is the volumetric airflow rate through the Deposition Box and Δt is the individual exposure duration. Concentration estimates were normalised using the corresponding sampled air volume, following the approach described by Ferrero et al. (2022). Overall mean concentrations and standard deviations for AMPs and TSMP were calculated from the 46 volume-normalised environmental sample concentrations, excluding laboratory blanks 11 and 12.

Once the collection was complete, the slides were immediately sealed in aluminium foil containers. The prepared samples were then transported to the laboratory for visual examination under a Leica M205C stereomicroscope.

2.2.2 Marine sampling

Seawater was collected using a 4 L metal bucket, which was flushed and cleaned with purified water before use. It was then poured through a 32 µm mesh stainless steel laboratory sieve. The material retained on the sieve was carefully transferred into pre-cleaned glass containers sealed with metal lids.

Water samples were collected at three different locations on Hanimaadhoo Island:

- the northern coast, at the closest possible distance from the measurement station (approximately 80 m in a straight line, indicated as point A on Fig. 1),
- the north-western coast (approximately 150 m from the measurement station, indicated as point B on Fig. 1),
- the central-western part of the island, adjacent to the local marina (indicated as point C on Fig. 1).

In addition, to verify the spatial distribution of MMPs pollution, seawater samples were also collected on other islands in the Maldives archipelago: Kelaa, Thuraakunu, Gan, and Hulhumalé (marked with the letters E, F, G1, G2, and H in Fig. 1).

A total of 15 MMPs samples were collected. The range of filtered water was 27–80 dm^3.

The collected MMP samples were initially stored in 100 mL glass vials containing the original suspension. These bottles were placed in an oven and dried at 60 °C for 48 h. Once dried, the samples were transported to the laboratory for further processing. At this stage, 30 % hydrogen peroxide (H_2O_2) was added to each bottle – ranging from 25 to 50 mL, depending on the volume lost to evaporation – to oxidise organic matter. The samples were then subjected to a second drying cycle at 60 °C for an additional 48 h, allowing further evaporation and decomposition of organic contaminants that otherwise could interfere with the analysis.

To isolate suspended materials, water samples were vacuum-filtered on glass fibre filters (Macherey-Nagel, grade MN 85/70, pore size 0.6 µm, diameter 55 mm), which were pre-heated at 450 °C for 4 h to remove potential contaminants.

To facilitate visual detection of particles on the filters, each sample was divided in half and thoroughly mixed before being poured into the Büchner funnel. During the decantation process, some sediment grains adhered to the container walls. After filtration, each filter was placed into a glass Petri dish and dried in an oven at 60 °C. To prevent cross-contamination, the Büchner funnel was cleaned after every one to two filtrations.

Finally, the dried filters were examined under a Leica M205C stereomicroscope for visual identification and analysis of MP particles.

2.3 Optical identification

During microscopic analysis, strict precautions were taken to minimise the risk of AMP contamination. All procedures were conducted under a laboratory fume hood. Prior to examining each sample, the microscope and surrounding work surfaces were thoroughly cleaned with a paper towel moistened with water. To assess the potential for background contamination, three clean Petri dishes were exposed near the microscope for 24 h. The number of fibres detected in these control dishes was 18, 20, and 29, respectively – equating to a contamination rate of less than one fibre per hour – thus considered negligible for the integrity of the results.

All samples were visually inspected under a Leica M205C stereomicroscope, and suspected MP particles were photographed at the highest achievable magnification (ranging from 7.8× to 160×) using an attached Leica DFC450 camera (5-megapixel resolution, 2560 × 1920 pixels, 3.4 × 3.4 µm pixel size). Each particle was then categorised by colour and shape, and its dimensions (length and width) were measured using the ImageJ software. The measurement of fibre length and width was conducted by means of the segmented line tool. Each fibre width was measured three to five times and averaged. For other particles, the polygon selection tool was used to outline them, enabling measurement of Feret diameters.

For airborne samples, TSMP denotes the particle population collected on the glass slides and detected during microscopic inspection. AMPs comprise the subset classified

as plastic using the optical-screening and spectroscopic procedures described here and in Sect. 2.4. Operationally, non-fibrous particles were included as MPs when their maximum dimension was ≤ 5 mm; elongated fibres were retained up to a length of 15 mm when their length-to-width ratio exceeded 3. The AMP population represented in the reported concentrations had measured lengths of approximately 32–6920 µm and widths of 6–410 µm. Concentrations and AMP contributions to TSMP are specific to this sampling and analytical workflow and may be affected by size-dependent collection, visual detection and material identification.

In the final phase of the study, selected marine and airborne samples were prepared for Raman spectroscopy to confirm the plastic nature of the particles and identify their polymer composition. During microscopic observation, the most distinctive items were marked with a pencil for marine samples and a 0.2 mm marker for airborne samples to clearly define the areas targeted for spectroscopic analysis.

Microscopy-derived particle data, including particle-size and morphology analyses, were processed and statistically analysed using R version 4.3.3 (R Core Team).

Equivalent aerodynamic diameters were estimated from microscopy-derived particle lengths and widths using the randomly oriented prolate-spheroid approximation described by Gonda and Abd El Khalik (1985), following Ferrero et al. (2022):

$$D_{\mathrm{ae}} = \sqrt{\frac{3}{2}} \cdot d \cdot \sqrt{\frac{\frac{\rho}{\rho_0}}{\frac{0.385}{\ln(2\beta)-0.5} + \frac{1.230}{\ln(2\beta)+0.5}}}. \quad (1)$$

Here, (d) is the measured particle width, $\beta = L/d$ is the aspect ratio, L is the measured particle length, and ρ is the material density. The reference density was $\rho_0 = 1000\,\mathrm{kg\,m^{-3}}$. Material densities of 955, 905, 1350, and $1130\,\mathrm{kg\,m^{-3}}$ were assumed for PE, PP, PET, and PA, respectively. These values represent model-derived estimates dependent on the assumed density, geometry, and orientation. For irregular fragments, the prolate-spheroid representation constitutes a geometric approximation. Aerodynamic diameters were estimated only for particles with assigned material densities; aspect-ratio summaries retained all particles with valid dimensions.

2.4 μ-Raman analysis

Raman spectroscopy was employed to identify the polymer type of suspected microplastic particles. Measurements were performed using a LabRam Aramis (Horiba Jobin Yvon) 460 mm spectrometer integrated with a confocal microscope. Two excitation sources were used: a diode-pumped solid-state laser at 532 nm (green) and a He-Ne laser at 632.8 nm (red). Spectra were recorded over a range of 400–3200 $\mathrm{cm^{-1}}$ with a spectral resolution of 2 $\mathrm{cm^{-1}}$. For each measurement, 20 scans of 2 s each were collected. A diffraction grating with 600 grooves $\mathrm{mm^{-1}}$ and a confocal aperture (hole) of 200 µm was employed.

Particles were initially located under a 10× objective (numerical aperture 0.25), and individual spots were scanned using a 50× objective (numerical aperture 0.5), focusing the laser on a 1–2 µm area of the particle. Neutral density filters (optical density 0–2) were applied as needed to adjust the laser intensity. Spectral data were processed using the LabSpec software (Horiba) and compared with reference spectra from literature for polymer identification.

Successful spectral matching for airborne samples was constrained by several practical and material-specific factors, including (i) occasional particle loss during transport, (ii) fluorescence and/or advanced weathering that obscured diagnostic Raman bands, and (iii) the use of two excitation wavelengths (532 and 632 nm), which do not provide equally effective performance across all polymer classes and non-polymeric materials. For this reason, polymer identification was not based exclusively on spectral-library matching. Instead, assignments were made primarily through manual interpretation of diagnostic Raman bands in individual spectra. Where library comparison was possible and informative, only matches of at least 70 % were accepted; nevertheless, the majority of identifications relied on direct expert spectral interpretation rather than on automated matching alone. Polymer attribution was based on direct Raman confirmation whenever achievable and, where appropriate, complemented by a conservative morphology-guided assignment for visually comparable particles collected under the same sampling conditions – an approach considered justified only when a shared provenance is plausible (Perraki et al., 2024).

Morphology and colour were used as first-pass screening criteria to separate candidate plastics from organic and mineral matter (often brown and beige). Plastic fibres were typically characterised by uniform width and sharp, cut-like edges. A useful observation from this study is that fibres with a lint-like surface texture were frequently identified as PE by Raman spectroscopy. In contrast, cellulose fibres often displayed variable width, split/elongated edges, and a twisted-ribbon appearance. Fragments displayed either lint-like PE-type textures or smooth surfaces with adhered dust; films appeared as small foil-like pieces. Representative particles are shown in Appendix B (Figs. B1 and B2).

In some marine samples, Raman spectra were dominated by pigments, complicating polymer-level identification. In such cases, particles were treated as "plastic/unclassified" only when spectral features and morphology together supported a plastic origin.

2.5 Meteorological and Aerosol measurements

Wind speed and direction were measured using a Gill WindMaster Pro sonic anemometer mounted at the top of the tower, 18 m above ground level (a.g.l.). Relative humidity, air temperature, and rainfall were monitored using a Vaisala

Weather Transmitter (WXT520), co-located at 18 m a.g.l., with a 3 min time resolution.

At MCOH, aerosol optical properties are monitored continuously. In the present study, aerosol absorption coefficients and instrument-estimated eBC (Petzold et al., 2013) were measured using a Magee Scientific AE33 aethalometer. The absorption data were corrected for filter multiple-scattering effects following Drinovec et al. (2015) and Ferrero et al. (2024). In this manuscript, eBC was derived from channel 6 (880 nm) of the AE33 and is used as a qualitative tracer of anthropogenic aerosol influence and regional atmospheric transport. No fossil-fuel versus biomass-burning source apportionment was applied to the aethalometer data, because such separation depends strongly on assumed source-specific absorption Ångström exponents and ideally requires independent validation, for example by radiocarbon-based ^{14}C source apportionment (e.g., Gustafsson et al., 2009).

Aerosol light scattering was measured using an integrating nephelometer (TSI Model 3563), which provided scattering coefficients at 450, 550, and 700 nm. Scattering data were corrected for truncation error following Müller et al. (2011). In the present study, the scattering coefficient at 550 nm was used for comparison with AMP observations.

Aerosol sampling was carried out through a PM_{10} inlet located at 15 m a.g.l. Ambient air was drawn through a vertical sampling line from the inlet to the aerosol instrumentation installed in the laboratory at the base of the tower. Further technical details on aerosol sampling at MCOH are provided by Corrigan et al. (2006) and Budhavant et al. (2018).

The aethalometer and nephelometer datasets were screened for instrumental artefacts and physically unrealistic values before averaging to the time base used for comparison with AMP samples. Periods affected by instrument instability, maintenance, invalid flow conditions, or obvious short-term spikes unrelated to ambient variability were removed. However, the data-cleaning procedure applied here was not identical to the most recent site-specific MCOH quality-control protocol used for long-term aerosol-climatology studies. Accordingly, the aerosol variables are interpreted primarily as campaign-scale contextual indicators and as tracers of co-variability with AMP concentrations, rather than as a standalone long-term aerosol dataset. This distinction is particularly relevant for absolute eBC and scattering values, whereas the directional contrasts discussed below are used mainly as supporting evidence for changes in air-mass influence.

Meteorological and aerosol data processing, including quality control, temporal averaging, and statistical analysis, was performed using MATLAB R2020b (version 9.9; The MathWorks, Inc., Natick, MA, USA).

3 Results and discussion

The field campaign was carried out during the dry phase of the winter monsoon, when north-easterly winds originating over the Indian subcontinent prevail (Budhavant et al., 2018, 2024; Ramachandran and Rupakheti, 2020). During this season, the arriving air masses often bear signatures of South Asian winter pollution as they traverse the Indian Ocean before reaching the Maldives (Budhavant et al., 2018, 2023; Dasari et al., 2025). In addition to the monsoon-driven synoptic flow, local sea breezes and weak trade winds frequently develop around the islands. At the same time, regional ocean currents, influenced by monsoonal circulation, tend to remain relatively steady during the dry period. Although this season is generally characterised by scarce rainfall and stable temperatures – typical of the Maldives' equatorial setting, short-lived convective events and isolated thunderstorms may still occur, especially when local atmospheric conditions favour rapid vertical development. Below, detailed results are reported.

3.1 Microplastic concentrations

3.1.1 Airborne microplastics

AMPs accounted for approximately 9 % of TSMP. Among the 158 identified AMPs, fragments were slightly more abundant (86 particles; 54.4 %) than fibres (72 particles; 45.6 %). AMP concentrations ranged from 0 to 10.28 m^{-3}, with a mean of 3.06 ± 2.75 m^{-3} (mean $\pm$ standard deviation). Thus, AMPs were consistently present, but at low concentrations relative to the total suspended microparticle load, which was dominated by non-plastic material, notably cellulose. Detailed sampling results are provided in Appendix B (Table B2; Fig. B3).

Figure 2 compares the mean AMP concentration observed here with previously published regional datasets. The MCOH mean exceeds those reported for the East Indian Ocean (Wang et al., 2020), Sri Lanka (Perera et al., 2022), and the Sundarbans (Ghosh et al., 2025) by nearly an order of magnitude or more, while remaining closest to the coastal Arabian Sea values reported by Kaushik et al. (2024). In this sense, the low fractional contribution of AMP to TSMP should not be interpreted as evidence of negligible atmospheric contamination, but rather as a consequence of the strong non-plastic background typical of coastal and marine air masses. This interpretation is consistent with Perera et al. (2022), who showed that only a relatively small fraction of visually selected outdoor airborne particles in Sri Lanka were ultimately confirmed as synthetic. In contrast, natural and semi-synthetic materials dominated the remainder.

At the same time, the absolute AMP concentrations observed here were substantial relative to the available literature from the Indian Ocean sector. They exceeded those reported for the northeast Arabian Sea by Kaushik et al. (2024), who measured mean concentrations of $1.30 \pm 0.14\,m^{-3}$ in 2016 and $1.46 \pm 0.12\,m^{-3}$ in 2020. They were markedly higher than the outdoor values reported from Sri Lanka by Perera et al. (2022) (0.00–$0.23\,m^{-3}$). They were also above the open-ocean East Indian Ocean concentrations reported by Wang et al. (2020) (0.4 ± 0.6 items per $100\,m^3$) and the PM_{10} bound concentrations reported for the Sundarbans mangrove system by Ghosh et al. (2025) (10 ± 6 MPs per $100\,m^3$). Accordingly, although AMP represented only a modest fraction of TSMP, their abundance in air was comparatively elevated relative to several marine and coastal benchmarks from the wider Indian Ocean region.

These comparisons should be interpreted cautiously because the available studies differ in sampling design, sample size fraction, air volume, filter material, and analytical workflow. Even so, a consistent regional pattern emerges: AMP levels are strongly shaped by source proximity, population density, and atmospheric setting. Very low concentrations in the East Indian Ocean (Wang et al., 2020) and in low-density coastal Sri Lankan sites (Perera et al., 2022) indicate strong dilution in marine air masses and limited local input, whereas higher concentrations in coastal Goa (Kaushik et al., 2024) and in the present study imply either stronger regional source influence, weaker dilution, or both.

The broader South Asian literature supports this interpretation. In Sri Lanka, the highest outdoor AMP abundances occurred near industrial and high-density areas, while no AMP were detected in some low-density coastal settings (Perera et al., 2022). Ghosh et al. (2025) likewise showed that, even at a remote mangrove island, atmospheric MP concentrations responded strongly to mesoscale meteorological conditions, with higher values during land-breeze and fog-influenced periods. Rao et al. (2025) further reported higher AMP concentrations in summer than in winter, attributing this to enhanced photodegradation and resuspension under warmer, drier, and windier conditions. Similar mechanisms may also operate in the Maldives, where high solar radiation, salt exposure, and episodic strong winds may promote fragmentation and intermittent aerosolisation despite the marine influence. By contrast, passive deposition studies in megacities report orders-of-magnitude higher loads (Tauhiduzzaman et al., 2025). However, such flux-based datasets are not directly comparable with active air concentrations expressed in m^{-3}.

Taken together, the available literature indicates that the Maldives AMP dataset does not represent a weak atmospheric signal. On the contrary, it documents a morphologically mixed, slightly fragment-dominated, PE/PP-rich AMP assemblage with concentrations that are high relative to several currently available Indian Ocean and South Asian marine and coastal studies (Wang et al., 2020; Perera et al., 2022; Kaushik et al., 2024; Ghosh et al., 2025; Rao et al., 2025). At the same time, the low AMP contribution to TSMP shows that these MPs were embedded within a much larger background of non-plastic atmospheric material. We therefore infer that AMPs occurred in most environmental samples at concentrations elevated relative to several regional studies, but that they constituted a small proportion of the detected suspended microparticle population.

3.1.2 Marine microplastics (MMP)

In seawater, the operational marine dataset comprised 663 particles. MMP number concentrations ranged from 120 to $2656\,MP\,m^{-3}$, with a mean of $876 \pm 804\,MP\,m^{-3}$. Fibres accounted for 52 % of the identified particles, while fragments accounted for 48 %. Concentrations were calculated by dividing the number of MMPs identified in each sample by the volume of seawater filtered. Twelve highly elongated fibres measuring 5.18–9.13 mm were retained in the primary dataset according to the operational size criterion defined in Sect. 2. Applying the conventional upper size limit of 5 mm to all particle shapes reduced the mean concentration to $856 \pm 794\,MP\,m^{-3}$ but did not affect the overall interpretation of the results. Detailed site-specific sampling results are presented in Fig. B4 in Appendix B.

The highest concentrations occurred in sample 6 ($2656\,MP\,m^{-3}$, collected at the MCOH station) and sample 7 ($2060\,MP\,m^{-3}$, collected at Undhoali Beach near the marina), both sampled after a storm and both characterised by a high fragment fraction. This pattern is consistent with storm-related mechanisms that can increase observed MP abundance, including resuspension of nearshore material, redistribution of floating and neutrally buoyant particles, and mobilisation of coating fragments from vessels or infrastructure. A third high value was observed in sample 9 ($2060\,MP\,m^{-3}$) near Thuraakunu Island, the most western site in this dataset. While this is less intuitive in a simple distance-from-source framework, it is consistent with the idea that concentrations at individual sites may be shaped by advection, local circulation, or episodic transport, rather than solely by immediate proximity to inhabited shorelines. The lowest concentrations were found in samples 12 and 14 ($180\,MP\,m^{-3}$ at the Gan and MCOH stations, respectively) and in sample 15 ($120\,MP\,m^{-3}$ at Hulhumalé Beach). Because these low values were observed at different coastal locations, no simple spatial gradient emerged. Filtered volume did not correlate with concentration, although smaller volumes typically increase counting uncertainty and can amplify sample-to-sample variability.

Figure 3a further emphasises that the MMP signal was highly heterogeneous across sites, with no simple monotonic spatial trend. Instead, the distribution was characterised by sharp local maxima, particularly in the post-storm samples, superimposed on a background of substantially lower concentrations. This pattern supports the interpretation that

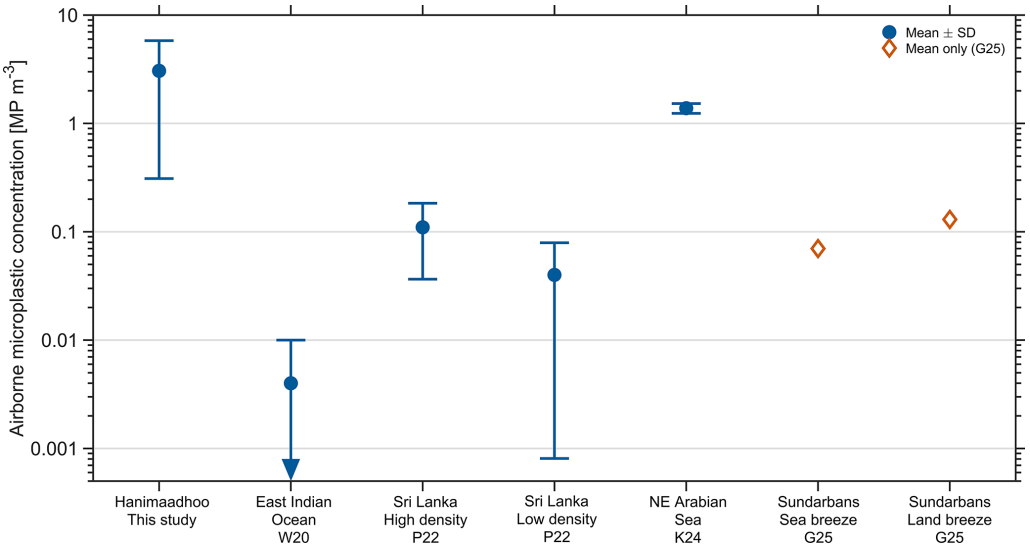

Figure 2. Regional comparison of airborne microplastic (AMP) concentrations. Circles show means ± SD. P22 SDs were converted from SEs; K24 statistics were recalculated from four samples collected in 2016 and 2020. G25 diamonds show means only because the dispersion statistic is undefined. The arrow mark the truncated W20 lower SD whisker. W20 – Wang et al. (2020); P22 – Perera et al. (2022); K24 – Kaushik et al. (2024); G25 – Ghosh et al. (2025).

MMP abundance around the Maldives is controlled by a combination of local inputs and short-term redistribution processes rather than by distance from inhabited shorelines alone. In addition, at the Hanimaadhoo site, where repeated sampling under contrasting tidal conditions was available, a potential influence of tide height on MMP concentration was observed. Mean concentrations were substantially higher during high tide (1360 ± 882 MPs m^{-3}) than during low tide (409 ± 194 MPs m^{-3}). Although a similar pattern was not evident at the other sites, those locations were represented only by singular sampling events, which preclude an equivalent assessment of tidal effects. The Hanimaadhoo results suggest that local hydrodynamic conditions, including tidal stage, may influence nearshore MMP abundance through changes in water exchange, resuspension, and particle redistribution within the coastal zone.

For comparison with previous studies, Fig. 3b presents all concentrations in a harmonised unit of items m^{-3}. On this basis, the mean concentration observed here (876 ± 804 MPs m^{-3}) is substantially higher than the values reported in the available Indian Ocean literature. The contrast is particularly strong with the two Maldivian studies of Saliu, which reported an average surface-water concentration of 0.26 particles m^{-3} in Faafu Atoll in 2018, with site values ranging from 0.02 to 0.48 particles m^{-3}, and in a subsequent survey reported mean values of 0.46 ± 0.15 items m^{-3} inside the atoll rim and 0.12 ± 0.09 items m^{-3} outside the reef.

The present values are also clearly above those reported by Athapaththu et al. (2020) for southern coastal Sri Lanka, who found a mean microplastic density of 17.45 ± 3.35 items m^{-3} in surface waters, and by Hildebrandt et al. (2022) for the tropical Indian Ocean, who reported 8–132 MP m^{-3} with a mean of 50 ± 30 MP m^{-3} for the 20–300 µm fraction, while the > 300 µm fraction averaged only 0.1 ± 0.4 MP m^{-3}.

Accordingly, Fig. 3b shows that the concentrations measured in the present study are higher than those reported in the comparison datasets by roughly one to two orders of magnitude relative to Athapaththu et al. (2020) and Hildebrandt et al. (2022), and by several orders of magnitude relative to the Maldivian seawater values of Saliu et al. (2018, 2019).

This difference likely reflects not only environmental forcing but also methodological contrasts among studies. A particularly important factor in the present work is that seawater was directly poured through a 32 µm stainless-steel laboratory sieve, which likely enhanced the recovery of the smallest particles and increased the total number of items. This is important because many Indian Ocean seawater studies rely on manta or neuston nets with substantially larger mesh sizes, typically 150–500 µm, and such approaches inevitably underrepresent the fine end of the microplastic size spectrum.

Even with this methodological divergence, the comparison strongly suggests that the present Maldives dataset does not represent a low-level open-ocean background. Rather, it indicates a markedly elevated nearshore MMP burden, consistent with strong local anthropogenic inputs associated with inhabited islands, coastal infrastructure, tourism, and maritime activity, as well as episodic storm-driven and tidal redistribution processes. The potential influence of the Indian Ocean "garbage patch" was also considered (Connan et al., 2021). Although this accumulation zone contains high levels of plastic macro-debris, studies with overlapping sampling areas do not necessarily report elevated MP concentrations in

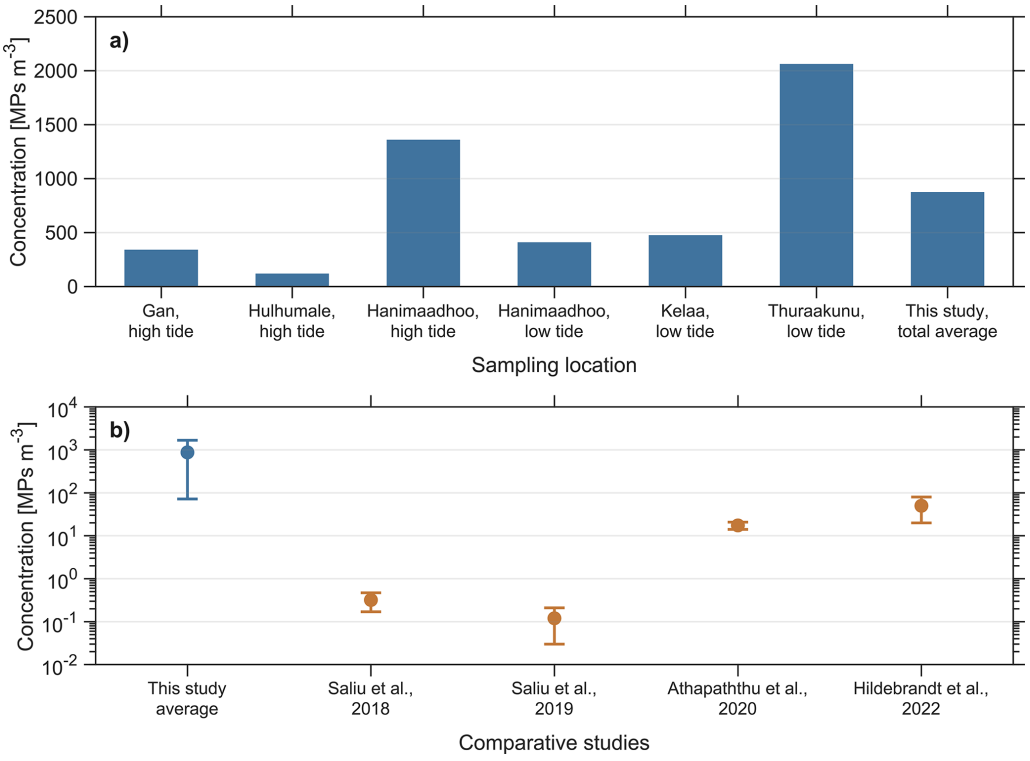

Figure 3. Spatial variability and regional comparison of marine microplastic (MMP) concentrations. **(a)** MMP concentrations were measured at the individual sampling sites in the Maldives study area. **(b)** Comparison of mean MMP concentrations (±standard deviation) from the present study with values reported in previous studies from the Indian Ocean region.

surface waters and therefore do not support it as the dominant explanation for the high abundances observed here. Instead, the site-specific peaks in Fig. 3a and the broader contrast shown in Fig. 3b indicate that MMP concentrations around the Maldives are more strongly influenced by local anthropogenic inputs and short-term hydrodynamic forcing than by large-scale oceanic accumulation zones.

Taken together, these results indicate that MMP concentrations around the Maldives are highly variable in space and time and are shaped by a combination of local source strength, storm-related remobilisation, and, at least at Hanimaadhoo, a probable tidal control on nearshore particle abundance. In this context, the present dataset appears to reflect a coastal-island system in which MP concentrations are driven primarily by local anthropogenic influence and episodic redistribution processes. The comparison with previous Indian Ocean studies is further complicated by substantial differences in sampling resolution, particularly regarding the lower size limit retained.

3.2 Microplastic dimensions and shape

Quantifying the dimensions of MP particles is central to their classification and interpretation, including whether particles fall within the formal MPs size definition and how efficiently they may be transported and deposited in the atmosphere or aquatic environment (Arthur et al., 2009; European Commission, 2011; Zeng, 2023). Non-fibrous particles were classified as MPs when their maximum dimension was ≤ 5 mm. Owing to their highly elongated geometry, fibres were retained up to a length of 15 mm when their length-to-width ratio exceeded 3. Twelve marine fibres measuring 5.18–9.13 mm and one airborne fibre measuring 6.92 mm met this criterion. A sensitivity analysis was additionally performed using the conventional 5 mm upper size limit for all particle shapes.

Recorded TSMP lengths ranged from 18 to 7670 µm, and widths from 2 to 624 µm. Corresponding AMP lengths ranged from 32 to 6920 µm, and widths from 6 to 410 µm. These observed dimensional ranges do not, by themselves, establish a validated lower detection limit or demonstrate complete detection of particles at the smallest recorded sizes.

The AMP length distribution was strongly right-skewed (Fig. 4a), with an overall mean of 546 µm and a median of 297 µm. This pooled distribution reflects the contrasting dimensions of the two principal morphologies rather than a numerical dominance of short fibres. Fragments, which accounted for 54.4 % of the identified AMPs, were substantially shorter, with a mean length of 251 µm and a median of 216 µm. Fibres were less numerous but considerably longer, with a mean length of 899 µm and a median of 526 µm,

and therefore contributed disproportionately to the upper tail of the distribution. The concentration of observations in the sub-millimetre range may be consistent with fragmentation and weathering at the source, followed by morphology-dependent aerodynamic selection during atmospheric transport. However, particle dimensions alone cannot distinguish conclusively between these processes or identify a specific source.

The overall mean AMP length observed in the present study was close to the mean particle sizes of 525–538 µm reported by Kaushik et al. (2024) and somewhat lower than the mean of approximately 643 µm reported by Wang et al. (2020) for the East Indian Ocean. For fibres specifically, the present median of 526 µm was close to the value of 551 µm reported by Perera et al. (2022), whereas the mean fibre length of 899 µm was higher than that reported by Perera et al. (2022; 769 µm) but lower than the fibre means of approximately 1086–1125 µm reported by Kaushik et al. (2024). Consequently, the present dataset does not provide evidence for a general enrichment in short fibres. Instead, its relatively low overall median primarily reflects the substantial contribution of comparatively short fragments. These comparisons should nevertheless be interpreted cautiously because the studies differed in sampling design, lower detection limits, and particle-identification procedures.

The AMP width distribution showed two clearly separated groups (Fig. 4c), but this structure was associated predominantly with particle morphology. Fibres were generally narrow, with a mean width of 15.9 µm and a median of 15.0 µm, whereas fragments were substantially broader, with a mean width of 132.8 µm and a median of 110.2 µm. Of the 73 particles narrower than 32 µm, 70 were fibres, while 83 of the 85 particles wider than 32 µm were fragments. Thus, the broad-width group should not be interpreted primarily as a separate population of thick technical fibres or rope-derived filaments. Instead, the width distribution largely reflects the coexistence of narrow, elongated fibres and broader fragments.

This morphological separation may nevertheless have implications for atmospheric transport. Narrow fibres can potentially remain suspended efficiently because of their elongated geometry and relatively low settling velocity, whereas broader fragments would generally be expected to undergo more rapid gravitational removal. Such behaviour also depends on particle density, orientation, surface roughness, and atmospheric turbulence. The observed width structure therefore supports a morphology-dependent difference in transport efficiency, but it does not by itself demonstrate that the broader particles originated locally or that the narrower fibres were transported over longer distances.

The marine fraction was nearly balanced, with fibres accounting for 52 % of MMPs and fragments for 48 %. This near-even partition indicates that seawater contained both elongated and non-elongated particles in comparable proportions. In the broader Indian Ocean context, that balance is plausible. The recent Indian Ocean review shows that fibres and fragments are the two dominant MP forms in seawater across the basin, with fibres contributing about 53 % and fragments about 34 % in non-trawl sampling studies, and slightly more balanced proportions in trawl-based datasets. Athapaththu et al. (2020) reported that filaments were the dominant morphotype in southern coastal Sri Lanka, while Li et al. (2022) also identified fibres as the dominant shape in the southern Indian Ocean. Thus, the present MMP morphology is consistent with regional evidence, but with a higher fragment share than the most fibre-dominated coastal datasets.

MMP size distributions were strongly right-skewed and heterogeneous (Fig. 4b and d). Much of the observed size structure was associated with particle morphology. Fibres were substantially longer, with a mean and median length of 1284 and 923 µm, respectively, and narrower, with a mean and median width of 16 and 12 µm. Fragments were shorter (mean: 119 µm; median: 90 µm) and broader (mean: 59 µm; median: 50 µm).

The broad MMP size range remains consistent with observations from the Indian Ocean, although direct comparison is complicated by differences in sampling and analytical methods. Athapaththu et al. (2020) found that more than 45 % of MPs in southern Sri Lankan coastal waters were < 1 mm, with more than 25 % in the 400–600 µm range. Li et al. (2022) reported that the most common size class in the southern Indian Ocean was 500–1000 µm (38.5 %), followed by 100–500 µm (28.85 %). They reported a size range of 108–4703 µm and an average particle size of 1060 ± 991 µm, overlapping with much of the fibre-size range observed in the present study.

By contrast, Hildebrandt et al. (2022) reported a much finer distribution in the tropical Indian Ocean: 75 % of the detected MPs were in the 20–50 µm range, 21 % were in the 50–100 µm range, and 96 % were < 100 µm. This difference probably reflects both methodological and environmental factors. Hildebrandt et al. (2022) sampled subsurface water at 6 m depth and targeted very small particles using highly sensitive fractionated filtration, whereas the present study focused on nearshore waters and retained a broader particle-size spectrum. Direct comparison is therefore meaningful only when differences in sampling depth, mesh size, and analytical size limits are considered.

The MMP width distribution likewise primarily reflected morphological differences rather than two independently fitted particle populations. The narrow fraction was dominated by fibres, whereas fragments and coating-derived particles contributed mainly to the broader fraction. This separation may be related to differences in particle production, hydrodynamic behaviour, and environmental retention. Nevertheless, particle dimensions alone cannot demonstrate particle origin or distinguish conclusively between local fragmentation, transport, and remobilisation processes.

Overall, AMP and MMP size distributions primarily reflected differences between fibrous and fragment-like particles. Fibres generally formed the narrower and longer frac-

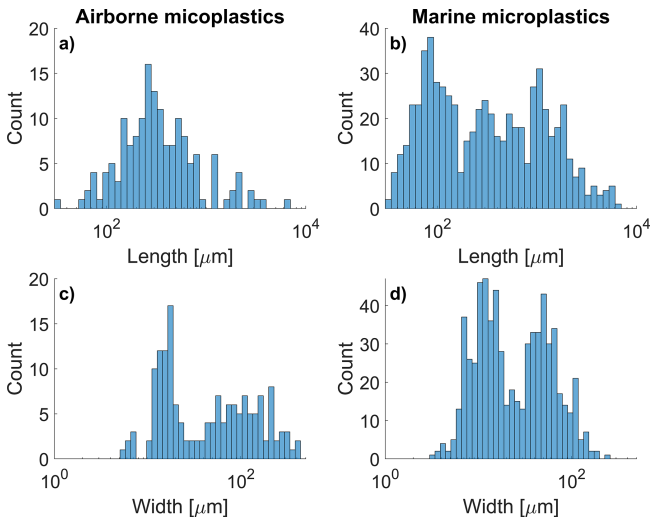

Figure 4. Size distributions of airborne and marine microplastics (AMP and MMP) shown on logarithmic scales. The upper panels present **(a)** AMP length distribution and **(b)** MMP lengths. The lower panels present **(c)** AMP width distribution and **(d)** MMP width distribution.

tion, whereas fragments formed the broader and shorter fraction. The two environmental compartments nevertheless differed significantly in their particle-size distributions, indicating that the atmospheric and marine assemblages were shaped by different combinations of particle morphology, transport, and environmental retention.

3.3 Polymer composition and morphological properties

Figure 5a, b shows the relative contribution of polymer types identified in AMPs and MMPs, respectively. In the airborne fraction, PE was the dominant polymer (51 % of identified AMP), followed by PP (28 %), PET (5 %), and polyamide (PA, 1 %); 15 % of AMPs could not be assigned because no sufficiently robust match was obtained in the μ-Raman analysis. This pattern broadly overlaps with South Asian atmospheric datasets, indicating that PE, PP, and PET are recurrent airborne polymers, although their relative proportions vary substantially across environments. For example, Ghosh et al. (2025) identified only four polymers in the Sundarbans atmosphere (PET, PE, PP, and polystyrene), with PP and PE dominating especially during sea-breeze conditions, whereas Rao et al. (2025) reported a Delhi NCR aerosol signal dominated by PET (41 %) and PE (27 %). In contrast, Perera et al. (2022) found that outdoor AMPs in Sri Lanka were dominated by PET (48 %), followed by polyester (PES, 34 %), PA (14 %), and acrylic (4 %), while Kaushik et al. (2024) reported a chemically distinct Arabian Sea aerosol signature dominated by polyvinyl chloride and polymethyl methacrylate, followed by PES and other polymers. Thus, the present airborne assemblage is not simply identical to previously reported coastal or island datasets, but is best described as a polyolefin-rich atmospheric mixture, with PE and PP clearly more prominent than in the Sri Lankan or Delhi datasets and far more prominent than in the Goa aerosol record (Kaushik et al., 2024).

The pie charts in Fig. 5 do not by themselves identify the source, and it would be too strong to state that the observed polymers are definitively packaging- or fishing-derived. It can be said that the AMPs' polymer pattern is consistent with that of common secondary consumers and of maritime plastics. That inference is based on the known uses of these polymers and on comparison with the literature, not on the pie charts alone. PE and PP are widely used in packaging, household items, ropes, and fishing-related materials; PET is common in textiles, bottles, films, and packaging; and PA is frequently associated with textiles, ropes, and nets. In this sense, the present AMPs spectrum is consistent with a mixture of widely used low-density consumer plastics and maritime materials, but it is not diagnostic of a single source class.

This distinction is important, particularly because the Sri Lankan study interpreted its PET-rich airborne signal mainly in terms of textile sources, while Ghosh et al. (2025) linked PP- and PE-rich atmospheric particles to a mixture of fishing-net material, packaging waste, and marine or coastal reservoirs under contrasting breeze regimes. The present results suggest a mixed marine-coastal-atmospheric source pool, but they do not allow direct apportionment among packaging, fisheries, and other uses.

A further point that deserves explicit discussion is that the observed contrast between atmosphere and seawater may reflect not only different source regimes, but also different particle properties. In particular, PE and PP are low-density polyolefins and are more likely to remain at or near the sea surface, where they are more available for wind-driven resuspension and sea-spray-mediated exchange. By contrast, PET and PA are denser polymers, so they are more likely to remain suspended in the water column, sink, or be removed from the atmosphere more efficiently when present as compact fragments. Thus, the lower PET proportion in AMP and the higher PET proportion in MMPs may indeed reflect, at least in part, differential environmental partitioning and source differences. This does not prove that the observed air–water contrast is controlled primarily by density, but it does mean that the contrast should not be interpreted as purely source-driven. Rather, the observed distribution likely reflects the combined effects of source regime, polymer density, buoyancy, particle size, and shape-dependent deposition behaviour.

Figure 5b shows that the marine fraction was compositionally distinct from the airborne one. For the MMP analysed by μ-Raman, the material composition was dominated by paint particles containing dye (32.5 %) and PET (24.4 %), unclassified plastic particles (18.4 %), and polycarbonate (13.9 %). Smaller contributions were made by polypropylene (5.6 %), polyamide (4.5 %), and polyethylene (0.8 %). Several parti-

cles were categorised as unclassified plastic because dye or pigment signatures precluded confident polymer assignment, even though they were clearly plastic-like. The high contribution of paint-related particles is consistent with observations in the tropical Indian Ocean, where Hildebrandt et al. (2022) reported that acrylates/polyurethane/varnish-like particles accounted for 49 % of detected polymer clusters and PET for 26 %, with much smaller contributions from PP (8 %) and PE (4 %). In this respect, the present seawater dataset does not resemble a simple PE/PP-dominated open-water assemblage. Instead, it shows a strong enrichment in coating-like particles and PET, in good agreement with the Hildebrandt dataset.

A striking feature of the present MMPs dataset was the unusually high occurrence of pink fragments, which were brittle, intensely coloured, and visually consistent with paint chips. Raman spectra suggested the presence of a dye, likely rhodamine. Their predominance in post-storm samples supports the interpretation of localised emissions and mobilisation associated with storm-driven abrasion, as well as the release of material from marine coatings on vessels, harbour infrastructure, or coastal installations. The data support a substantial paint/coating contribution, but they do not identify a single unique source. A cautious interpretation is that coating-derived particles formed an important local source category in seawater and became particularly prominent after storm forcing.

The polymer distribution in the present seawater samples also differs from several broader reports from the Indian Ocean, in which PE and PP are described as among the dominant marine polymers. For example, a recent review of Indian Ocean monitoring data concluded that the main polymer types reported across the basin are PE, PP, and PS (Zhou et al., 2025), while another recent Indian Ocean study identified rayon, PE, PP, and PET as predominant materials (Wang et al., 2025).

Against that background, the strong prominence of paint-related particles and PET in the present MMPs appears distinctive, though not anomalous in light of Hildebrandt et al. (2022). The most likely explanation is that broad basin-scale syntheses integrate many settings dominated by diffuse consumer plastic inputs, whereas the present samples capture a more localised island-maritime signal, shaped by proximity to infrastructure and storm-enhanced mechanical release.

The observed contrast between airborne and marine particle classes may also have implications for hazard, although this point should be treated cautiously. Based on Fig. 5 alone, toxicity cannot be ranked reliably by polymer type, because hazard depends not only on the base polymer, but also on particle size, morphology, weathering state, additive content, pigment load, and sorbed contaminants (Prata et al., 2024). Even so, the dominant particle classes identified here are unlikely to be equivalent. The marine fraction, enriched in paint/coating particles, deserves particular attention because such materials are chemically complex and may contain pigments, dyes, stabilisers, and other additives (Turner, 2021). In contrast, elongated airborne particles can remain suspended and contribute to inhalation exposure (Eberhard et al., 2024). Accordingly, the present results do not support the view that all identified polymers have the same environmental or health relevance; rather, they suggest that risk likely varies among particle classes, even though that variability cannot be resolved quantitatively from the present dataset alone.

On the whole, the polymer data suggest a system in which the airborne fraction is dominated by common polyolefins, likely reflecting a mixed secondary-consumer and maritime-plastic signal, whereas the marine fraction is enriched in paint/coating-related particles and PET, indicating a stronger imprint of local maritime sources. However, this apparent contrast should not be attributed solely to source differences. Polymer-specific properties such as density, buoyancy, morphology, and deposition behaviour are also likely to influence whether particles are preferentially retained in air or seawater. At first glance, the behaviour of MPs appears partly decoupled between the atmosphere and the ocean, but this decoupling most likely reflects a combination of source regime and particle properties rather than a single factor. Further data supporting this interpretation are presented in the next section.

3.4 Air and marine microplastics comparison at MCOH site

In the preceding sections, microplastic properties were analysed using the full dataset, encompassing all sampling locations across the study area. In the following section, the analysis is restricted to a subset of samples collected in the immediate vicinity of the MCOH station. This approach ensures spatial consistency between airborne and marine datasets and enables a more direct comparison of their properties under comparable environmental conditions.

The dimensional distributions of AMP and MMP are compared in Fig. 6. For this analysis, the MMP data include only samples collected in the vicinity of the airborne measurement station to ensure spatial consistency between the two datasets (Sampling sites A and B in Fig. 1).

The length and width distributions of AMP and MMP differed substantially (Fig. 6). Within the MCOH subset used for this comparison, marine fibres had a median length of 930 µm and a median width of 11 µm, whereas marine fragments had a median length of 86 µm and a median width of 49 µm. Airborne fibres had corresponding median dimensions of 526 and 15 µm, while airborne fragments had median dimensions of 216 and 110 µm. Thus, the broad peaks visible in the distributions largely reflect the coexistence of fibrous and fragment-like morphologies rather than independently fitted statistical modes.

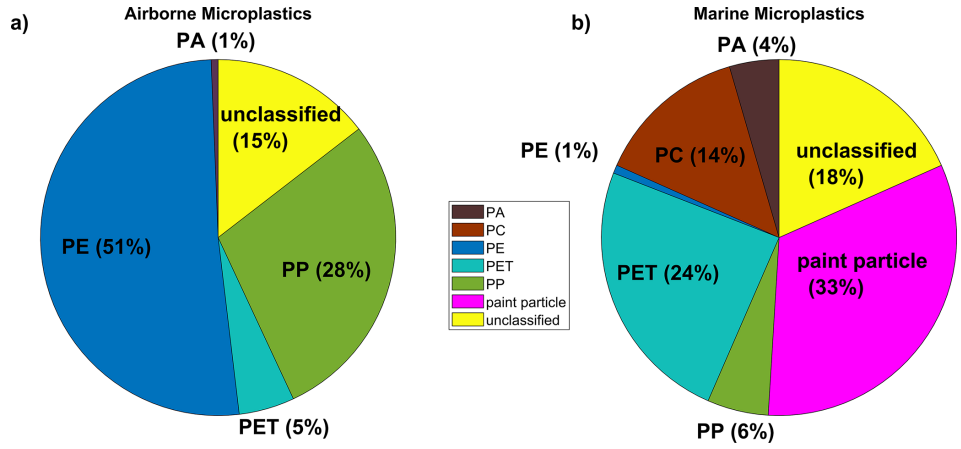

Figure 5. Relative abundance of polymer types among all identified microplastics: **(a)** airborne sampling polymer composition; **(b)** marine sampling polymer composition.

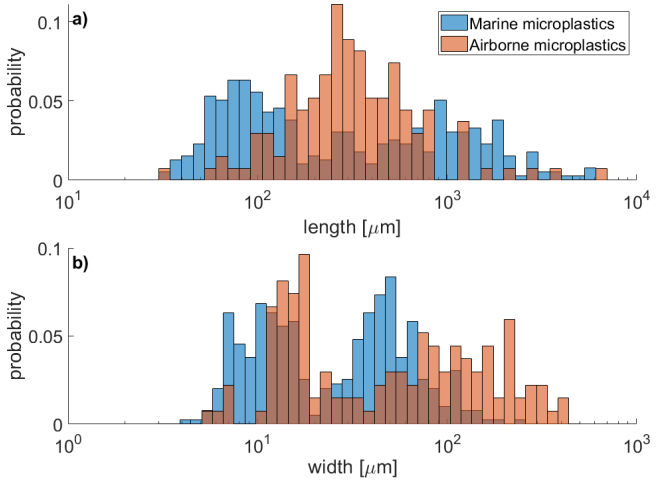

Figure 6. Probability distributions of particle dimensions for airborne and marine microplastics. Histograms compare airborne microplastics (orange) and marine microplastics (blue) measured during the campaign. Panel **(a)** shows the length distribution of microplastic particles, while panel **(b)** shows the width distribution.

To assess whether the length and width distributions of MMP and AMP differ statistically, we applied Kolmogorov–Smirnov tests. The results indicate that the two MP properties resulted with highly significant differences (p-values $< 10^{-8}$).

These differences can be interpreted in the context of environmental processes governing MP transport. Wind speed is a key control mechanism linking air-sea exchange, as it controls wave breaking, bubble entrainment, and sea spray aerosol production – all key pathways for MP transfer from the ocean to the atmosphere. Numerous studies have documented that sea spray aerosol fluxes increase sharply with wind speed due to enhanced turbulence and bubble-bursting activity (Lewis and Schwartz, 2004; O'Dowd and de Leeuw, 2007). Under high-wind conditions, such processes could entrain MP into the marine boundary layer (Allen et al., 2020; Ferrero et al., 2022). Conversely, during the dry season in the Maldives, mean wind speeds are very low, resulting in weak surface turbulence and minimal sea–air coupling.

These calm conditions strongly suppress the mechanisms responsible for upward MP transport, thereby reducing the likelihood that oceanic plastics contribute appreciably to the AMP population. Low winds likewise limit the atmospheric deposition of airborne particles onto the sea surface. Together, these factors indicate that the AMP sampled during our campaign likely originates from sources or processes decoupled from the immediate marine environment, rather than from local ocean-to-atmosphere exchange. Thus, the observed statistical differences between AMP and MMP size distributions reflect not only the inherent variability in MP sources and fragmentation processes but also the Maldives' environmental regime during the dry season. The weak wind forcing helps to explain why the two reservoirs appear largely disconnected, highlighting the importance of seasonal meteorological conditions when interpreting MP exchange across the air–sea interface.

To sum up, the statistical differences between AMP and MMP size distributions suggest that the two reservoirs were only weakly connected during the study period, highlighting the importance of seasonal meteorological conditions in regulating microplastic exchange across the air-sea interface.

3.5 Pattern of air mass advection

Meteorological conditions during the campaign were generally calm, with an average wind speed of $2.34 \pm 1.48\,\mathrm{m\,s^{-1}}$ and occasional stronger episodes, including a maximum gust of $12.48\,\mathrm{m\,s^{-1}}$ recorded on 23 January at 22:36 UTC. Precipitation was limited, although short periods of intense rain-

fall occurred, with the highest rate reaching 16.8 mm h^{-1} recorded on 24 January at 00:00 UTC. Aerosol loading exhibited substantial variability: the mean aerosol scattering coefficient at 550 nm was 47.6 ± 20.4 Mm^{-1}, peaking at 115.5 Mm^{-1} at 04:00 UTC on 23 January. The eBC concentrations were also elevated, averaging 1.75 ± 0.71 µg m^{-3}, with a maximum value of 3.7 µg m^{-3} observed at 07:00 UTC on 30 January 2023.

During the measurement campaign, the prevailing wind direction oscillated between the north-northwest and east sectors. These shifts in air mass origin were accompanied by differences in both TSMP and AMP characteristics. To explore variability under contrasting wind conditions, sampling windows were assigned to northerly (300–30°) and easterly (30–120°) sectors using the midpoint of the most frequent 1° wind-direction bin during each exposure. This distinction enables a more explicit examination of how changes in advected air masses affect the observed AMP concentrations. All AMP sample results are presented in Fig. 7 in a polar plot.

Figure 8 shows the descriptive distributions for all 46 environmental samples, including short and long exposures. The following inferential comparison used five non-overlapping short-exposure sampling windows per sector. Mean TSMP concentrations were 37.38 ± 12.50 and 46.46 ± 24.35 m^{-3}, respectively. Corresponding AMP concentrations were 3.10 ± 2.95 and 2.53 ± 2.50 MP m^{-3}. Values following ± represent standard deviations among sampling windows. Neither comparison was statistically significant (two-sided permutation tests using the Kolmogorov–Smirnov statistic: $p = 0.87$ for TSMP and $p = 0.81$ for AMP). The observations document variability within both wind sectors, but do not establish a systematic directional difference in AMP concentration.

Figure 9 presents pooled particle-level distributions from all environmental samples. Mean TSMP aspect ratios were 25.76 ± 34.21 under northerly flow and 27.33 ± 27.54 under easterly flow. Corresponding AMP aspect ratios were 29.25 ± 40.69 and 19.76 ± 32.73. Mean estimated AMP aerodynamic diameters were 95.67 ± 88.52 and 103.07 ± 98.99 µm, respectively. Values following ± denote particle-level standard deviations. A separate comparison based on window-mean aerodynamic diameters did not resolve a difference between sectors (exact two-sided permutation K–S test, $p = 0.97$; four northerly and three easterly windows). These descriptive differences characterise the collected particle populations but do not establish distinct sources or transport regimes.

In addition to concentrations and aerodynamic diameter, differences among polymer compositions were examined. PE was the most abundant assigned polymer in both sectors, accounting for 41.9 % of all AMPs under northerly flow and 62.5 % under easterly flow. PP contributed 31.4 % and 25.0 %, and PET 4.7 % and 5.6 %, respectively. Unclassified plastics were retained in these denominators.

Taken together, these comparisons document variability in the observed particle populations and provide hypotheses for further investigation of atmospheric microplastic transport. The sources and transport histories of AMPs remain unresolved.

3.6 Equivalent black carbon and aerosol scattering as anthropogenic tracers to MP

During the campaign, the mean eBC concentration was 1.75 ± 0.71 µg m^{-3}, and the mean aerosol scattering coefficient at 550 nm was 47.6 ± 20.4 Mm^{-1}. These values indicate that the study period was characterised by appreciable aerosol loading, consistent with the dry-season South Asian outflow regime previously documented at MCOH. Earlier work has shown that MCOH is an important receptor site for polluted South Asian air masses, including transport from the Indo-Gangetic Plain and surrounding source regions. For example, Budhavant et al. (2024) reported substantial processing of black and brown carbon during transport over the Indian Ocean, while Nair et al. (2023) showed that eBC at MCOH is sensitive to changes in South Asian emissions and decreased markedly during the COVID-19-related emission reductions. In this context, the eBC levels observed during the present January–February 2023 campaign are consistent with a polluted wintertime receptor regime rather than with a clean marine background.

The comparison in Fig. 10 further illustrates the relationship between air-mass advection, eBC, and aerosol scattering. Both variables show higher values under northerly advection than under easterly advection, consistent with the AMP patterns discussed above. Mean eBC concentrations were 1.94 ± 0.86 µg m^{-3} for northerly flow and 1.41 ± 0.65 µg m^{-3} for easterly flow. Aerosol scattering showed a similar directional contrast, with higher values under northerly advection (51.0 ± 22.4 Mm^{-1}) than under easterly advection (36.1 ± 12.8 Mm^{-1}). The corresponding violin plots, together with the confidence intervals, indicate that the northerly sector was associated with a systematically stronger aerosol signal overall.

These aerosol observations provide context for the conditions under which AMPs were collected. eBC indicates combustion-derived aerosol influence, whereas light scattering characterises the broader aerosol population. The AMP concentration comparison did not resolve a systematic contrast between wind sectors. Consequently, the aerosol measurements support an exploratory interpretation of the atmospheric setting, but do not independently establish common sources or transport pathways for AMPs.

At the same time, the two tracers should not be interpreted in the same way. eBC is more directly linked to combustion-derived emissions and is therefore useful as an indicator of anthropogenic input, whereas aerosol scattering integrates a wider range of particle types, including both anthropogenic aerosol and natural components such as sea spray and min-

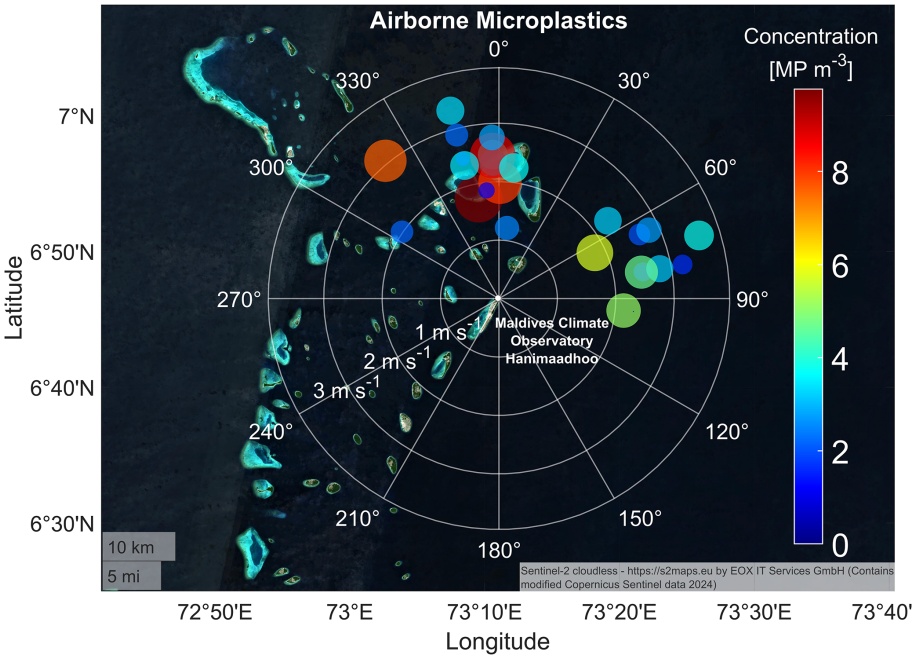

Figure 7. Airborne microplastic (AMP) concentrations plotted against wind conditions during the corresponding Deposition Box sampling exposures. Angular position indicates the prevailing wind direction, with north at 0° and east at 90°, while radial distance from the plot centre represents wind speed in m s^{-1}. Circle size and colour encode AMP concentration in MP m^{-3}. The satellite basemap shows Hanimaadhoo and neighbouring Maldivian islands and atolls; the turquoise and bluish irregular features represent reefs and shallow coastal or lagoon waters. The satellite basemap provides geographical context. Circle positions represent wind conditions during sampling. Satellite-image attribution is provided within the figure.

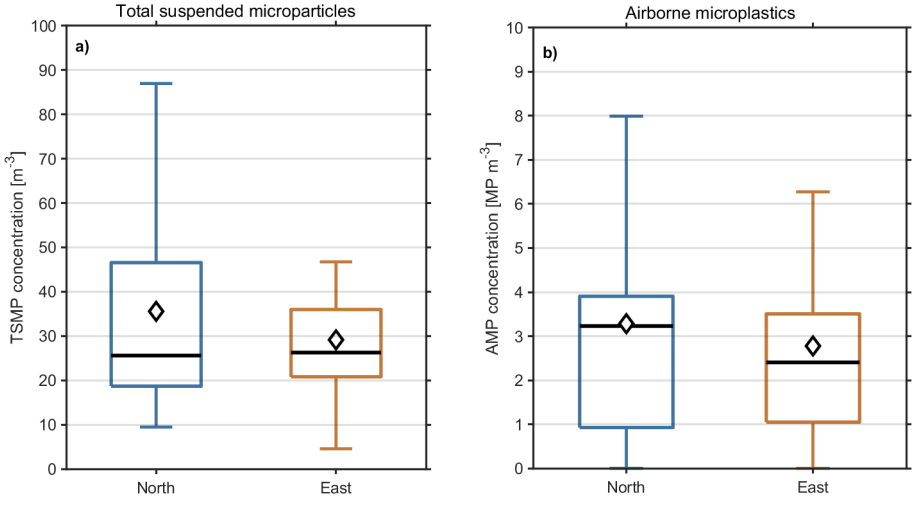

Figure 8. Total suspended microparticles **(a)** and airborne microplastics **(b)** concentrations under northerly and easterly flow for all 46 environmental samples. Boxes span the interquartile range, black lines indicate medians, and white diamonds indicate arithmetic means. Whiskers extend to the most extreme observations within 1.5 times the interquartile range from the box edges.

eral dust. For this reason, scattering should be regarded as a broad indicator of total aerosol loading rather than as a specific tracer of microplastic sources. The sectoral differences in aerosol optical properties provide context for the atmospheric conditions encountered during AMP sampling.

The higher abundance of eBC, aerosol scattering and AMP concentration during the northerly wind regime, coupled with the large particle size and therefore likely short atmospheric lifetime of the observed AMPs, may at first suggest an aerosol mass influenced by emissions from adjacent

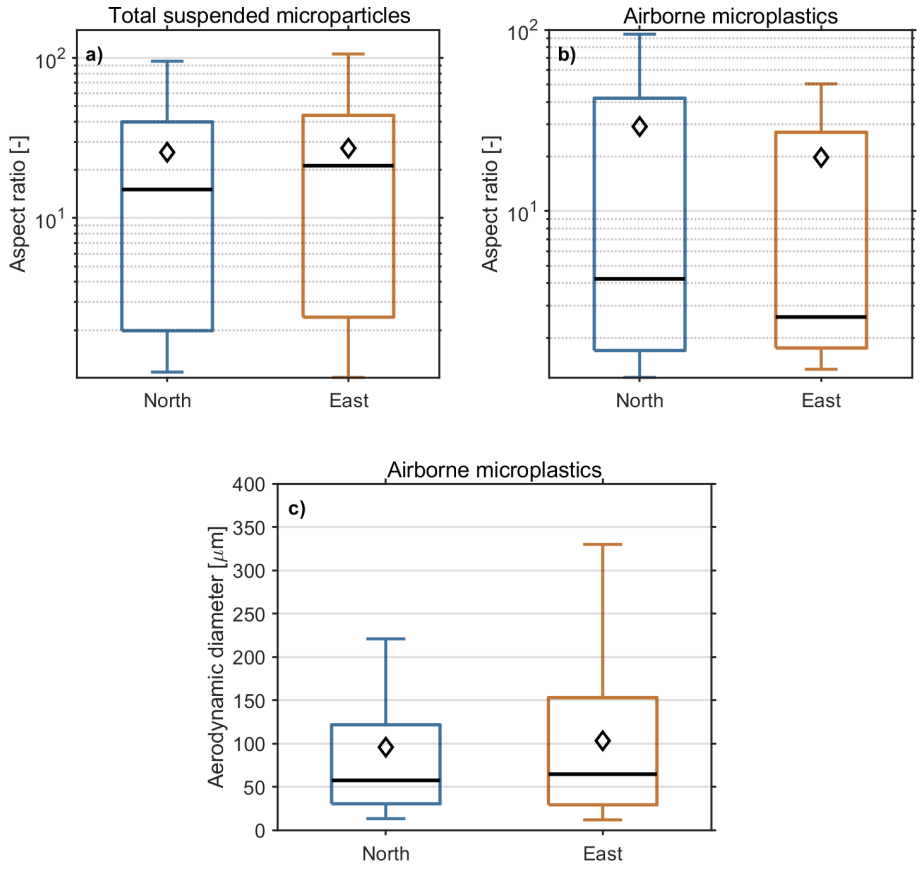

Figure 9. Distributions of total suspended microparticles aspect ratios **(a)**, airborne microplastics (AMP) aspect ratios **(b)**, and estimated AMP aerodynamic diameters **(c)**, using pooled particles from all environmental samples under northerly and easterly flow. Box plots prepared in the same convention as the Fig. 8.

islands to the north of Hanimaadhoo. However, concurrent observations of organic aerosol properties using an Aerosol Mass Spectrometer (Stegelius et al., 2026) did not reveal a signature of local emissions influencing the site from the north. In contrast, the chemical characteristics of aerosol observed during this campaign were broadly consistent, regardless of air mass history. Fresh, local emissions contributed less than 5 % to organic aerosol mass, and did not increase with northerly wind. The remainder demonstrated features characteristic of aged, transported aerosol. The aerosol population observed during this campaign therefore represents a largely secondary, regionally mixed, sulfate-rich and highly processed haze (Stegelius et al., 2026). Previous studies support this interpretation carried out at this site, which indicate that aerosol observed at MCOH during the winter has undergone extensive regional mixing and atmospheric processing during long-range transportation. The most prominent identified source region at this time of year is the Indian sub-continent (e.g., Budhavant et al., 2018, 2024; Spencer et al., 2008).

Higher AMP concentrations under northerly advection coincided with elevated eBC and aerosol light scattering. This co-variability indicates an association between AMP abundance and the observed aerosol and advection conditions, but does not establish common emission sources or determine AMP transport distances. The chemical evidence for aged, transported aerosol discussed above provides context for the aerosol background; it cannot be directly used to assign the origin or transport history of AMPs.

The joint AMP and aerosol measurements characterise the conditions encountered during sampling. However, the AMP comparison based on non-overlapping sampling windows did not resolve a systematic wind-sector contrast. The chemical evidence for aged, transported aerosol provides context for the aerosol background but cannot be used directly to assign the origin or transport history of AMPs.

Long-range atmospheric transport remains a plausible hypothesis, supported by observations of airborne microplastics in remote marine and Antarctic environments (Chen et al., 2023). Similarly, van der Does et al. (2018) reported that giant dust particles (> 75 µm) can be transported surprisingly vast distances, suggesting that the same may be possible for large AMPs. Contributions from local or regional AMP emissions superimposed on a transported aerosol background also

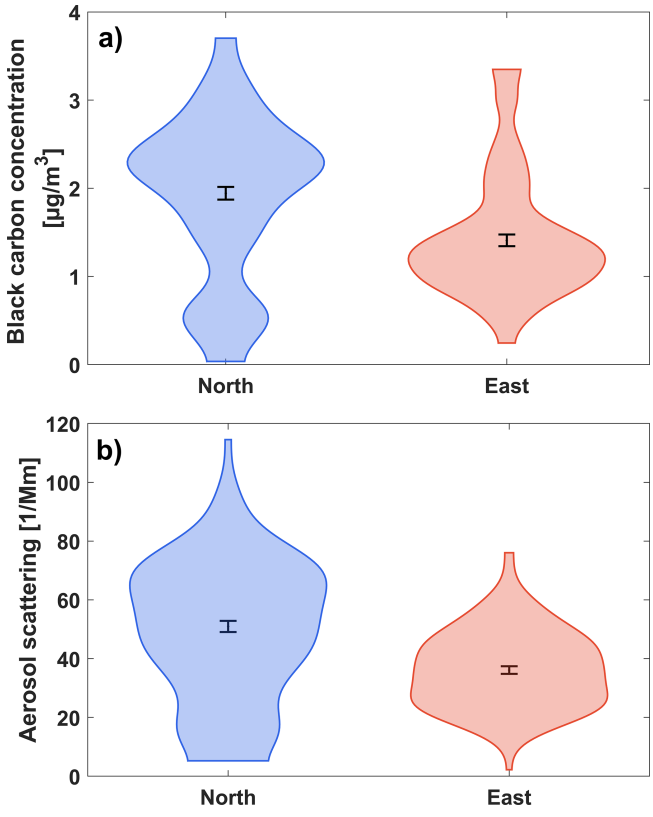

Figure 10. Violin-plot comparison of aerosol properties under contrasting air-mass advection regimes. Panel **(a)** shows equivalent black carbon (eBC) concentrations, and panel **(b)** shows the aerosol scattering coefficient at 550 nm, each separated into northerly and easterly advection patterns. The violin shapes represent the data distribution for each regime, central markers indicate mean values, and error bars denote the corresponding 95 % confidence intervals. Together, the plots illustrate the enhancement of both eBC and aerosol scattering under northerly advection relative to easterly flow.

cannot be excluded. The present observations do not distinguish these possible contributions or quantify their relative importance. Further source-specific measurements and transport analyses are required to evaluate these hypotheses.

4 Conclusions

This study provides a coupled assessment of MMPs and airborne AMPs in the northern Indian Ocean, based on intensive one-month observations conducted at the Maldives Climate Observatory Hanimaadhoo and in the surrounding coastal waters. By combining MP characterisation with aerosol optical measurements, the study characterises particle properties in a remote island environment and provides atmospheric context for interpreting AMP variability.

First, the concentration, size, colour, and polymer composition of both AMP and MMP were quantified. MMPs occurred at concentrations substantially higher than those typically reported for open-ocean regions, indicating a strong influence of local anthropogenic activity associated with inhabited islands, coastal infrastructure, and maritime operations. Both compartments showed broadly balanced fibre-to-fragment proportions, although fibres were slightly more abundant in the marine dataset, whereas fragments were slightly more abundant among AMPs. Polymer compositions were broadly consistent with regional studies, although the high contribution of paint- or coating-related fragments points to a distinct localised source likely linked to ship-related materials.

Second, comparison of AMPs and MMPs revealed pronounced and statistically significant differences in size distributions, indicating weak coupling between the two reservoirs during the observation period. The low wind speeds characteristic of the dry season likely suppressed air–sea exchange processes such as wave breaking and bubble bursting, thereby limiting ocean-to-atmosphere transfer of MPs. Under these conditions, the observed AMP population appears largely decoupled from the local MMP pool and instead more strongly influenced by terrestrial and coastal emission sources.

Third, elevated AMP concentrations coincided with enhanced eBC and aerosol light scattering under northerly advection. These measurements provide context for interpreting AMP variability in relation to aerosol and advection conditions. However, the observed co-variability does not establish common emission sources or a causal relationship between AMPs and combustion-derived aerosol. The present dataset does not allow definitive attribution of AMPs to local emissions, regional transport, or long-range transport, and their relative contributions remain unresolved.

Future campaigns could benefit from active aerosol sampling at higher volumetric flow rates, increasing the number of particles collected per unit time. This could reduce counting uncertainty and enable shorter collection intervals. Combined with a larger number of independent sampling periods, such measurements could improve temporal resolution and increase the statistical power of comparisons between advection regimes.

Taken together, these results show that MPs should be integrated into atmospheric transport frameworks rather than treated only as a marine pollution problem. They also demonstrate that remote marine atmospheres are not necessarily isolated from anthropogenic plastic aerosol transport, even in apparently ocean-dominated settings such as the Maldives. More broadly, combining AMP and MMP observations with meteorological and aerosol optical measurements can help interpret MP variability and guide further investigation of potential sources, atmospheric transport, and air–sea exchange processes in island environments. Integrating MP observations with established aerosol measurements will therefore be essential for improving our understanding of how plastic particles are transported through the atmosphere and redistributed across remote marine regions.

Appendix A: Acronyms

AMP	airborne microplastic
eBC	equivalent black carbon
MCOH	Maldives Climate Observatory Hanimaadhoo
MP	microplastic
MMP	marine microplastics
PA	polyamide
PC	polycarbonate
PE	polyethylene
PES	polyester
PET	polyethylene terephthalate
PM_{10}	Particulate Matter 10
$PM_{2.5}$	Particulate Matter 2.5
PP	polypropylene
PS	polystyrene
TSMP	Total suspended microparticles

Appendix B: Supporting tables and figures

Table B1. Basic statistical characteristics of aerosol and airborne microplastic sampling.

	median		mean		Standard deviation		Min–max		1st–3rd quartiles	
Advection type	N	E	N	E	N	E	N	E	N	E
TSMP, m^{-3}	25.59	26.27	35.57	29.14	28.58	18.36	9.46–133.53	4.56–88.17	18.68–46.56	20.80–35.98
AMPs, MP m^{-3}	3.23	2.40	3.28	2.78	3.00	2.43	0.00–10.28	0.00–7.62	0.93–3.90	1.05–3.51
eBC, µg m^{-3}	2.15	1.27	1.94	1.41	0.86	0.65	0.00–3.74	0.22–3.38	1.48–2.51	0.98–1.60
Scattering, Mm^{-1}	53.0	35.5	51.0	36.1	22.4	12.8	4.2–115.5	1.5–76.7	35.1–68.4	25.3–45.0
TSMP, Aspect ratio, –	15.09	21.25	25.76	27.33	34.21	27.54	1.09–338.47	1.01–198.67	1.98–39.87	2.41–43.82
AMPs, Aspect ratio, –	4.22	2.60	29.25	19.76	40.69	32.73	1.21–160.06	1.34–198.67	1.70–41.91	1.75–27.19
AMPs, aerodynamic diameter, µm	57	65	96	103	89	99	13–388	12–439	30–122	29–153

Table B2. Deposition-box sampling periods and exposure times.

AMP sample no.	start	stop	exposure time
	year-month-day time		days
1	23-01-13 07:18	23-01-14 08:15	1.04
2	23-01-13 07:18	23-01-15 09:20	2.08
3	23-01-13 07:18	23-01-17 06:00	3.95
4	23-01-13 07:18	23-01-17 06:00	3.95
5	23-01-13 07:18	23-02-04 07:00	21.99
6	23-01-13 07:18	23-02-04 07:00	21.99
7	23-01-13 07:18	23-01-19 06:45	5.98
8	23-01-13 07:18	23-01-19 06:45	5.98
9	23-01-13 07:18	23-01-27 07:14	14.00
10	23-01-13 07:18	23-01-27 07:14	14.00
11	23-01-13 07:40	23-02-04 07:00	21.97
12	23-01-13 07:40	23-02-04 07:00	21.97
13	23-01-14 08:15	23-01-19 06:45	4.94
14	23-01-15 09:20	23-01-17 06:00	1.86
15	23-01-17 06:00	23-01-19 06:45	2.03
16	23-01-17 06:00	23-01-19 06:45	2.03
17	23-01-17 06:00	23-01-21 06:45	4.03
18	23-01-19 06:45	23-01-21 06:45	2.00
19	23-01-19 06:45	23-01-21 06:45	2.00
20	23-01-19 06:45	23-01-23 05:30	3.95
21	23-01-19 06:45	23-01-23 05:30	3.95
22	23-01-19 06:45	23-01-25 12:40	6.25
23	23-01-21 06:45	23-01-25 12:40	4.25
24	23-01-21 06:45	23-01-23 05:30	1.95
25	23-01-21 06:45	23-01-23 05:30	1.95
26	23-01-23 05:30	23-01-27 07:14	4.07
27	23-01-23 05:30	23-01-24 08:30	1.13
28	23-01-23 05:30	23-01-25 12:40	2.30
29	23-01-23 05:30	23-01-25 12:40	2.30
30	23-01-24 08:30	23-01-27 07:14	2.95
31	23-01-25 12:40	23-01-27 07:14	1.77
32	23-01-25 12:40	23-01-29 07:10	3.77
33	23-01-25 12:40	23-01-31 06:54	5.76
34	23-01-25 12:40	23-02-02 07:00	7.76
35	23-01-27 07:14	23-01-29 07:10	2.00
36	23-01-27 07:14	23-01-29 07:10	2.00
37	23-01-27 07:14	23-01-31 06:54	3.99
38	23-01-27 07:14	23-02-02 07:00	5.99
39	23-01-27 07:14	23-02-04 07:00	7.99
40	23-01-29 07:10	23-01-31 06:54	1.99
41	23-01-29 07:10	23-02-02 07:00	3.99
42	23-01-29 07:10	23-02-04 07:00	5.99
43	23-02-02 07:00	23-02-04 07:00	2.00
44	23-02-02 07:00	23-02-04 07:00	2.00
45	23-02-02 07:00	23-02-04 07:00	2.00
46	23-01-31 06:54	23-02-04 07:00	4.00
47	23-01-31 06:54	23-02-04 07:00	4.00
48	23-01-25 12:40	23-02-04 07:00	9.76

Table B3. The list of marine samples.

MMP sample no.	Date and time of sampling	sampled volume, L	Sampling place	latitude	longitude	tide level
1	15-01-23 11:45	36	MCOH north	6°46′37.76″ N	73° 11′1.41″ E	high tide
2	15-01-23 12:45	27	MCOH west	6°46′32.98″ N	73° 10′54.50″ E	high tide
3	19-01-23 8:00	60	MCOH north	6°46′37.76″ N	73° 11′1.41″ E	low tide
4	21-01-23 9:45	64	MCOH north	6°46′37.76″ N	73° 11′1.41″ E	low tide
5	23-01-23 8:00	64	MCOH north	6°46′37.76″ N	73° 11′1.41″ E	high tide
6	24-01-23 11:00	64	MCOH north	6°46′37.76″ N	73° 11′1.41″ E	high tide
7	24-01-23 13:00	48	Undhoali Beach	6°46′5.89″ N	73° 10′29.89″ E	high tide
8	26-01-23 3:26	80	Kelaa	6°56′19.56″ N	73° 12′19.92″ E	low tide
9	26-01-23 7:14	48	Thuraakunu	7°6′23.28″ N	72° 53′14.82″ E	low tide
10	27-01-23 12:04	48	MCOH north	6°46′37.76″ N	73° 11′1.41″ E	high tide
11	29-01-23 14:30	40	Gan	0°41′15.71″ S	73°9′4.25″ E	high tide
12	31-01-23 14:00	44	Gan	0°40′58.92″ S	73°8′37.13″ E	moderate
13	02-02-23 12:30	52	MCOH north	6°46′37.76″ N	73° 11′1.41″ E	low tide
14	04-02-23 12:30	56	MCOH north	6°46′37.76″ N	73° 11′1.41″ E	low tide
15	07-02-23 9:15	50	Hulhumalé	4°12′51.74″ N	73° 32′43.53″ E	high tide

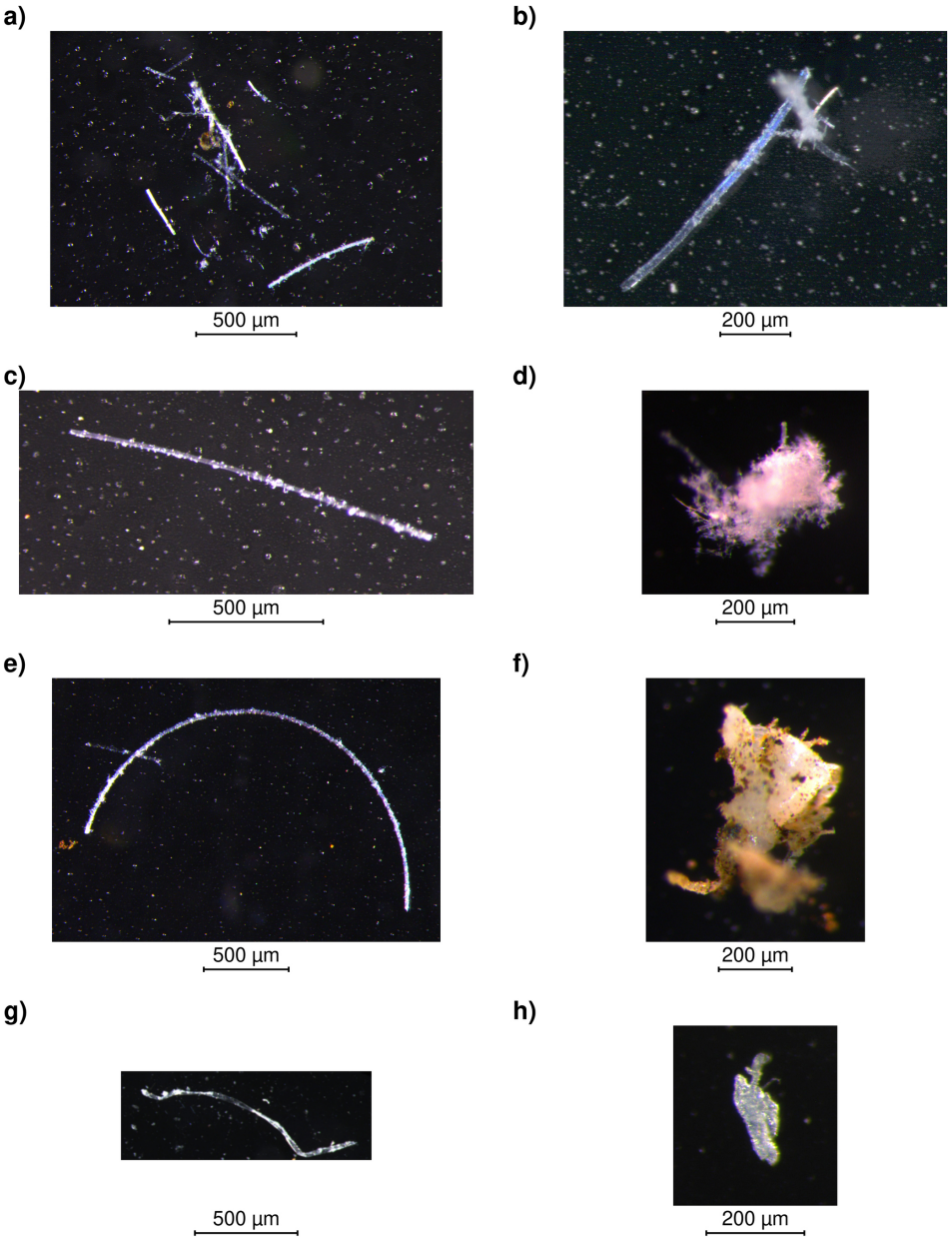

Figure B1. Representative airborne microparticles: **(a)** polyethylene (PE) fibres; **(b)** a polyethylene terephthalate (PET) fibre with an attached white PE fragment; **(c)** a PE fibre; **(d)** a PE fragment; **(e)** a PE fibre; **(f)** a polypropylene (PP) fragment; **(g)** a cellulose fibre; and **(h)** a PP film.

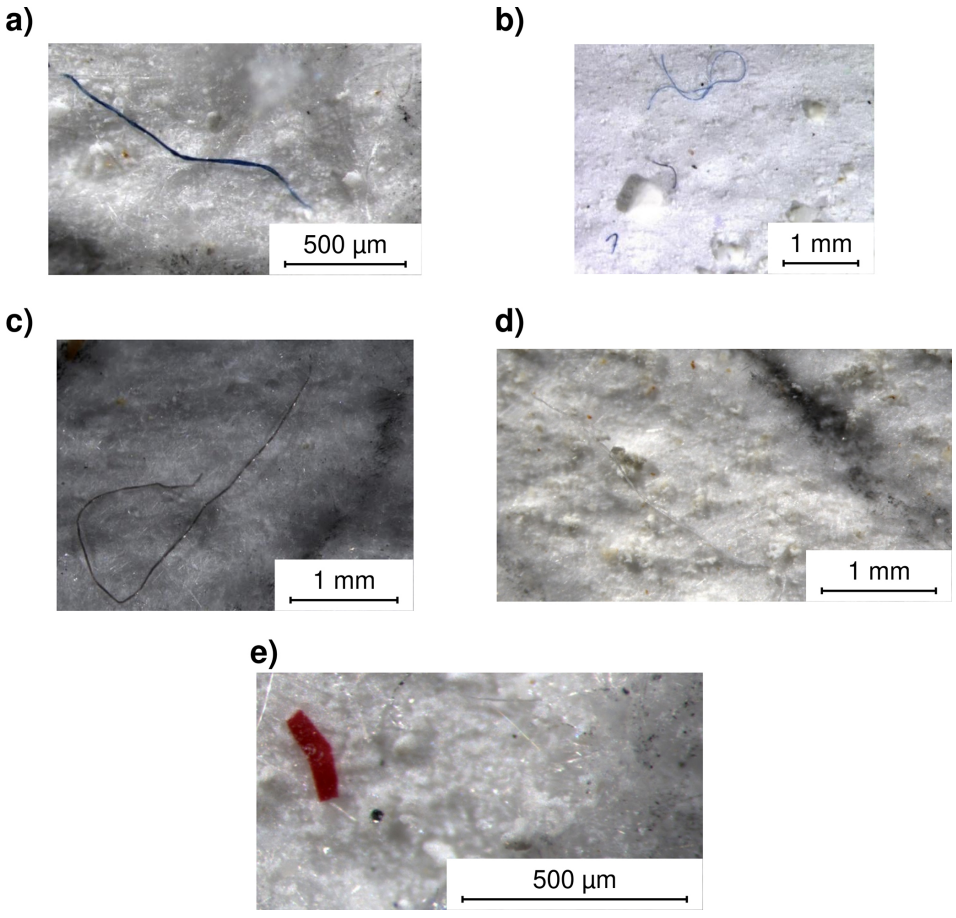

Figure B2. Representative marine microparticles: **(a, b)** blue polyethylene terephthalate (PET) fibres; **(c)** a brown PET fibre; **(d)** a transparent polypropylene (PP) fibre; and **(e)** a pink paint-related fragment containing dye.

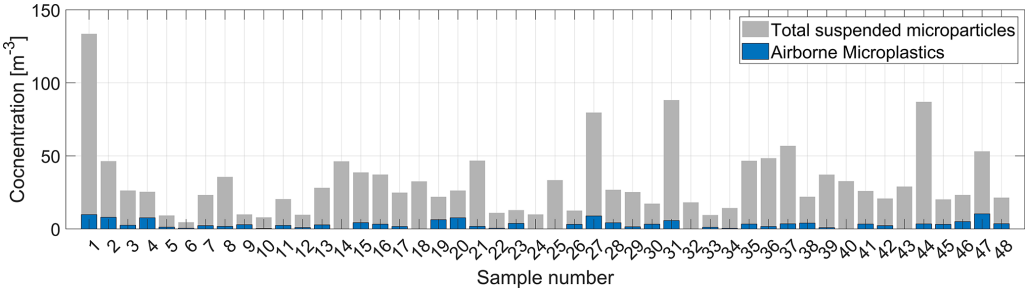

Figure B3. Number concentrations of total suspended microparticles (TSMP; grey bars) and airborne microplastics (AMP; blue bars) during the 48 deposition-box sampling periods at the Maldives Climate Observatory Hanimaadhoo (MCOH). 46 environmental samples and laboratory blanks 11 and 12; blanks were excluded from environmental statistics. TSMP comprises all detected microparticles, whereas AMP comprises the subset classified as microplastics using the optical-screening and spectroscopic-validation procedure described in Sect. 2.3 and 2.4. Consequently, the AMP concentration is included within, rather than additional to, the corresponding TSMP concentration.

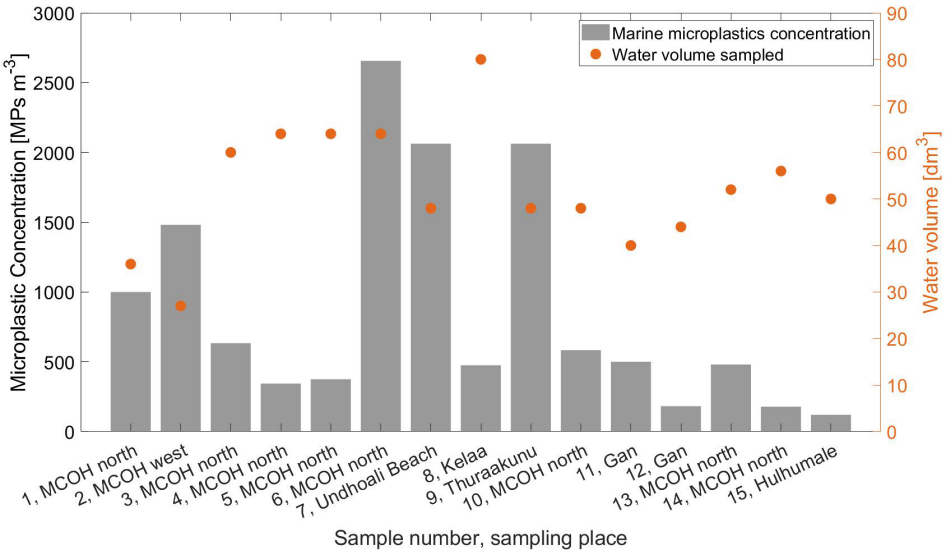

Figure B4. Concentrations of marine microplastics (MMP) were measured in seawater samples collected around the Maldives. Grey bars represent the microplastic concentration expressed as the number of particles per cubic metre (MP m^{-3}) for each sample (1–15). Orange circles indicate the volume of seawater filtered for each sample (dm^3), shown on the right vertical axis. Concentrations were calculated as the number of detected microplastic particles divided by the corresponding volume of filtered water. Variations in concentration partly reflect differences in local environmental conditions and sampling volume, including storm-driven resuspension and local coastal inputs.

Appendix C: Representative Raman spectra

C1 Scope and interpretation

This appendix presents representative Raman spectra of airborne and marine particles, including a cellulose comparison and examples dominated by colourants. The identification procedure is described in Sect. 2.4. AMP and MMP numbers denote collection samples. Raman shifts are given in cm^{-1} and intensities in arbitrary units (a.u.); spectral windows and intensity scales differ among examples.

Assignments consider combinations of bands and published spectra. Weathering and colourants can obscure polymer features (Dong et al., 2020; Azari et al., 2024). Colourant spectra do not identify the substrate polymer; tentative assignments are stated explicitly.

C2 Airborne particles

C2.1 Polyethylene

The purple fibre from sample AMP 48 was assigned to polyethylene (PE; Fig. C1). Bands near 1070, 1304, 1448 and 1470 cm^{-1} are consistent with C–C backbone stretching, CH_2 twisting and CH_2 deformation vibrations, respectively (Furukawa et al., 2006). The displayed window does not cover the principal C–H stretching bands near 2800–3000 cm^{-1}.

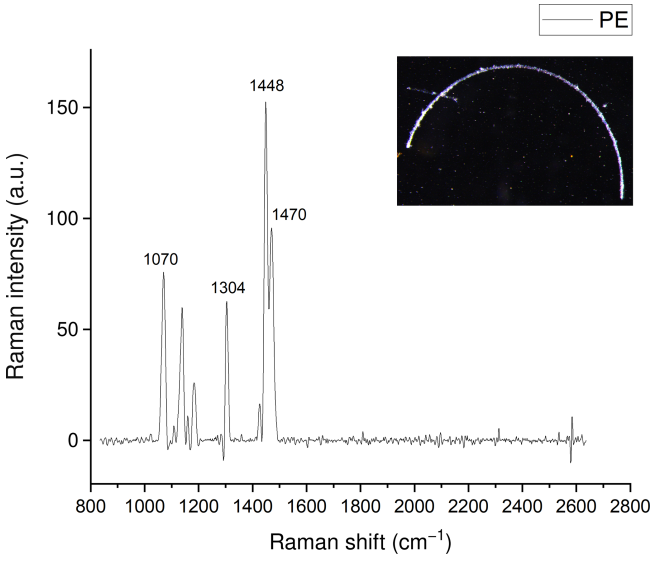

Figure C1. Measured Raman spectrum of a fibre assigned to PE from airborne sample AMP 48. The inset shows the analysed fibre.

The transparent fibre from sample AMP 13 has bands near 2843 and 2875 cm^{-1} (Fig. C2), consistent with the symmetric and asymmetric CH_2 stretching regions reported for PE (Furukawa et al., 2006; Rytelewska and Dąbrowska, 2022). The lower-wavenumber region provides limited additional diagnostic information.

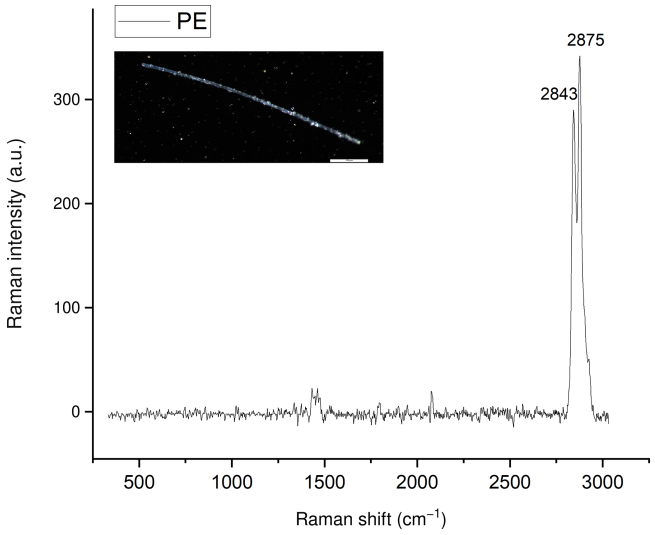

Figure C2. Measured Raman spectrum of a fibre assigned to PE from airborne sample AMP 13. The inset shows the analysed fibre.

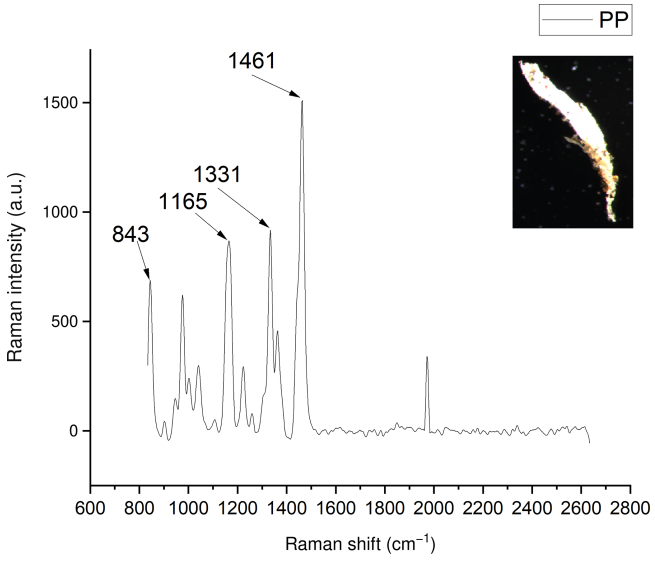

Figure C3. Measured Raman spectrum of a particle assigned to PP from airborne sample AMP 47. The inset shows the analysed particle.

C2.2 Polypropylene

The particle from sample AMP 47 shows bands consistent with polypropylene (PP; Fig. C3). Features near 843 and 946 cm^{-1} are associated with coupled skeletal vibrations and CH_3 rocking. The band near 1165 cm^{-1} occurs in the C–C stretching and C–H deformation region, while those near 1331 and 1461 cm^{-1} occur in the C–H and CH_2/CH_3 deformation regions (Andreassen, 1999; Furukawa et al., 2006). The combination of bands supports the assignment.

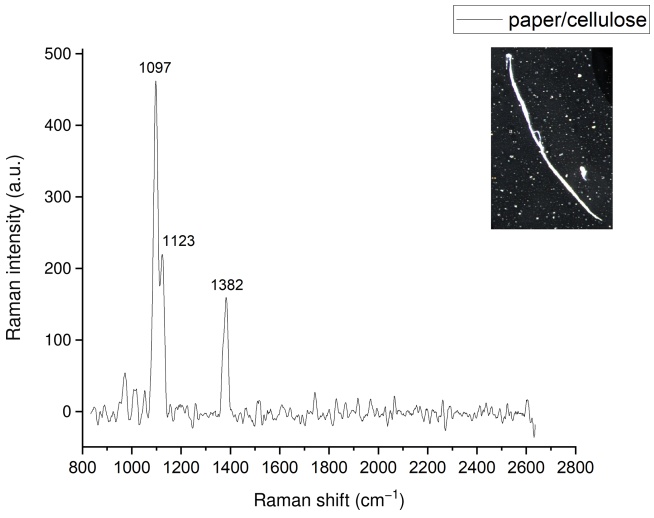

Figure C4. Measured Raman spectrum of a cellulose fibre from airborne sample AMP 8, shown as a non-plastic comparison. The inset shows the analysed fibre.

C2.3 Cellulose

A cellulose fibre from sample AMP 8 is shown as a non-plastic comparison (Fig. C4). Bands near 1097 and 1123 cm^{-1} are consistent with coupled C–O/C–C skeletal stretching, including glycosidic C–O–C contributions. The band near 1382 cm^{-1} occurs in a cellulose deformation region (Szymańska-Chargot et al., 2011; Agarwal et al., 2021). The spectrum does not distinguish a natural fibre from paper.

C2.4 Spectrum dominated by a colourant

The spectrum of the fibre from sample AMP 42 is dominated by a colourant (Fig. C5). Bands near 1191, 1276, 1344, 1458 and 1550 cm^{-1} overlap vibration regions reported for azo-containing colourants (Biswas and Umapathy, 2000; Castro et al., 2020). The comparison is qualitative: Castro et al. (2020) analysed extracted textile dyes, and the present spectrum does not establish an exact dye identity or the substrate polymer.

Fluorescence interference also depends on the excitation wavelength (Castro et al., 2020; Azari et al., 2024); the measurement procedure is described in Sect. 2.4.

C3 Marine particles

C3.1 Polyethylene terephthalate

The spectrum from sample MMP 9 shows bands near 854, 1614 and 1727 cm^{-1} (Fig. C6). The combination of a ring-related vibration, aromatic C=C stretching and ester C=O stretching supports the polyethylene terephthalate (PET) assignment (Peñalver et al., 2023).

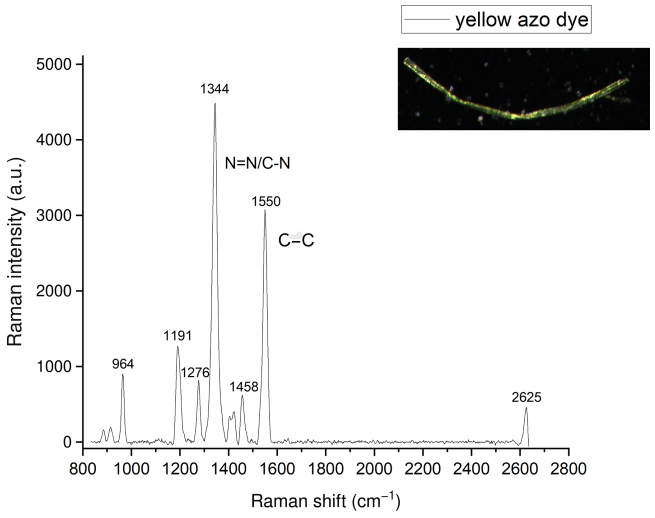

Figure C5. Measured Raman spectrum of a fibre from airborne sample AMP 42. The yellow azo dye label denotes a tentative colourant interpretation; the substrate polymer remains unresolved.

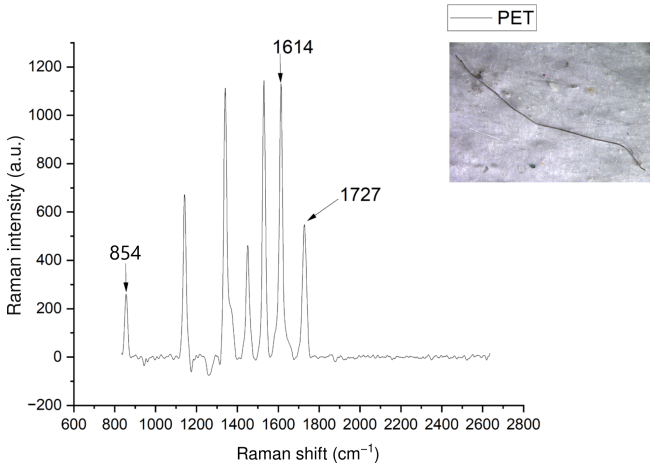

Figure C6. Measured Raman spectrum of a particle assigned to PET from marine sample MMP 9. The inset shows the analysed particle.

C3.2 Polypropylene

The spectrum from sample MMP 11 shows bands near 830 and 1452 cm^{-1} (Fig. C7), close to PP skeletal/CH_3 rocking and CH_2/CH_3 deformation bands, respectively (Guo et al., 2019). These selected bands are consistent with PP but are not individually diagnostic.

C3.3 Polyamide candidate with possible colourant interference

The coloured particle from sample MMP 9 has bands near 979, 1084, 1281 and 1445 cm^{-1} (Fig. C8), which overlap polyamide (PA) skeletal and deformation regions (Milani, 2015; Rytelewska and Dąbrowska, 2022). Prominent bands near 1214 and 1536 cm^{-1} remain unassigned, and possible colourant contributions limit the identification. PA remains a candidate assignment; the spectrum does not establish the PA type, such as PA6 or PA66.

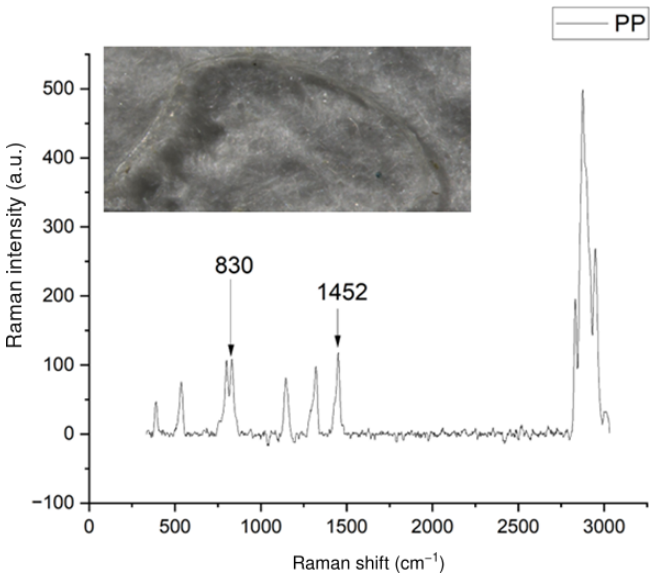

Figure C7. Measured Raman spectrum of a particle assigned to PP from marine sample MMP 11. The inset shows the analysed particle.

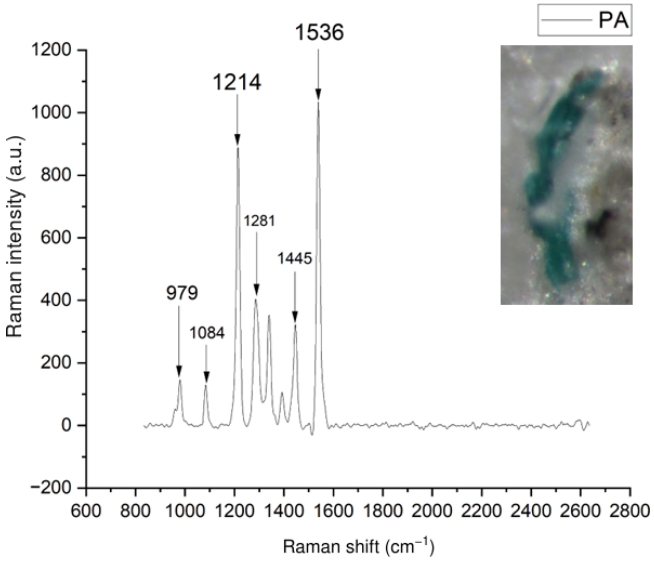

Figure C8. Measured Raman spectrum of the coloured particle from marine sample MMP 9. PA denotes a candidate assignment; colourant interference cannot be excluded.

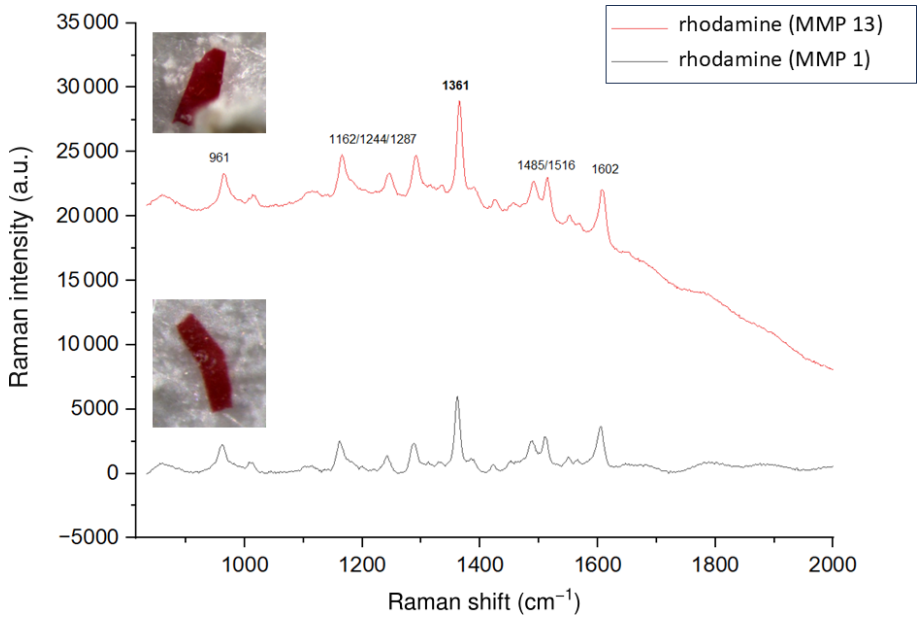

Figure C9. Measured Raman spectra and microscope images of pink fragments from marine samples MMP 13 and MMP 1. The rhodamine labels denote a tentative colourant interpretation; the substrate polymers remain unresolved.

C3.4 Spectra dominated by pink colourants

Spectra of pink fragments from samples MMP 13 and MMP 1 are dominated by colourant signals (Fig. C9), with selected bands near 961, 1287, 1361 and 1602 cm^{-1}. A rhodamine-like colourant remains a tentative interpretation. Liu et al. (2020) report a rhodamine B band near 1361 cm^{-1} using surface-enhanced Raman spectroscopy (SERS), which provides a qualitative comparison rather than a direct match. Although some features also overlap PP vibration regions, the substrate polymer remains unresolved.

Data availability. Data referenced in this study can be accessed via the Zenodo (https://doi.org/10.5281/zenodo.22102519, Markuszewski et al., 2026).

Author contributions. PiM, MM, LF, and DN conceptualised the study and designed the measurement campaign. PiM, SLH, and KB conducted the field measurements and sample collection. KS, MŚ, PJT, and AW performed the optical microscopy and μ-Raman analyses, including particle characterisation, polymer identification, and validation of the analytical results. LF, DN, MZ and ÖG supervised the research. KB provided access to the MCOH research infrastructure and coordinated local logistical support. PiM was responsible for project administration and funding acquisition. PiM curated and analysed the data, performed the statistical analyses, prepared the visualisations, and wrote the original draft of the manuscript. MM, KS, MŚ, PJT, LF, KB, MZ, AW, PrzM, DN, ÖG, and SLH contributed to the interpretation of the results and reviewed and edited the manuscript.

Competing interests. The contact author has declared that none of the authors has any competing interests.

Disclaimer. Publisher's note: Copernicus Publications remains neutral with regard to jurisdictional claims made in the text, published maps, institutional affiliations, or any other geographical representation in this paper. The authors bear the ultimate responsibility for providing appropriate place names. Views expressed in the text are those of the authors and do not necessarily reflect the views of the publisher.

Acknowledgements. The authors sincerely thank Sebastian Mahlik (Gdańsk University) for providing access to the Raman laboratory, where the Raman-based identification analyses presented in this study were carried out.

The authors acknowledge the support of Krzysztof Markowicz (Warsaw University), who advised us on the processing of aerosol properties data.

In addition, we thank the technical staff, Sharafulla Thoha, Mariyam, and Faruhaadh Moosa at MCOH, the Maldives Meteorological Service and the Government of the Republic of Maldives for their support during the field campaign.

This work is also an output of the GEMMA Centre in the framework of the project MUR TECLA "Dipartimenti di Eccellenza 2023–2027".

Grammarly was used to improve grammar, sentence structure and readability. ChatGPT also assisted with code preparation, data consistency checks and manuscript revision. All suggested changes were reviewed and approved by the authors, who retain full responsibility for the scientific content and final wording of the manuscript.

Figure 1b was produced with the Giovanni online data system, developed and maintained by the NASA GES DISC.

Financial support. This work was financially supported by the National Science Centre, Poland (Grant 2023/49/B/ST10/00513), the Polish National Agency for Academic Exchange (NAWA) under the Bekker NAWA programme (decision no. BPN/BEK/2024/1/00044/DEC/1), the Swedish Research Council (VR, Grant 2021-05225), and the Bolin Centre (under Research Theme 1).

Review statement. This paper was edited by Jurgita Ovadnevaite and reviewed by two anonymous referees.

References

Acker, J. G. and Leptoukh, G.: Online analysis enhances use of NASA Earth science data, Eos T. Am. Geophys. Un., 88, 14–17, https://doi.org/10.1029/2007EO020003, 2007.

Agarwal, U. P., Ralph, S. A., Baez, C., and Reiner, R. S.: Detection and quantitation of cellulose II by Raman spectroscopy, Cellulose, 28, 9069–9079, https://doi.org/10.1007/s10570-021-04124-x, 2021.

Allen, D., Allen, S., Abbasi, S., Baker, A., Bergmann, M., Brahney, J., Butler, T., Duce, R. A., Eckhardt, S., Evangeliou, N., Jickells, T., Kanakidou, M., Kershaw, P., Laj, P., Levermore, J., Li, D., Liss, P., Liu, K., Mahowald, N., Masque, P., Materić, D., Mayes, A. G., McGinnity, P., Osvath, I., Prather, K. A., Prospero, J. M., Revell, L. E., Sander, S. G., Shim, W. J., Slade, J., Stein, A., Tarasova, O., and Wright, S.: Microplastics and nanoplastics in the marine-atmosphere environment, Nat. Rev. Earth Environ., 3, 393–405, https://doi.org/10.1038/s43017-022-00292-x, 2022.

Allen, S., Allen, D., Phoenix, V. R., Le Roux, G., Durántez Jiménez, P., Simonneau, A., Binet, S., and Galop, D.: Atmospheric transport and deposition of microplastics in a remote mountain catchment, Nat. Geosci., 12, 339–344, https://doi.org/10.1038/s41561-019-0335-5, 2019.

Allen, S., Allen, D., Moss, K., Le Roux, G., Phoenix, V. R., and Sonke, J. E.: Examination of the ocean as a source for atmospheric microplastics, PLOS ONE, 15, e0232746, https://doi.org/10.1371/journal.pone.0232746, 2020.

Andreae, M. O. and Rosenfeld, D.: Aerosol–cloud–precipitation interactions. Part 1. The nature and sources of cloud-active aerosols, Earth-Sci. Rev., 89, 13–41, https://doi.org/10.1016/j.earscirev.2008.03.001, 2008.

Andreassen, E.: Infrared and Raman spectroscopy of polypropylene, in: Polypropylene: An A–Z Reference, edited by: Karger-Kocsis, J., Springer, Dordrecht, 320–328, https://doi.org/10.1007/978-94-011-4421-6_46, 1999.

Arthur, C., Baker, J., and Bamford, H. (Eds.): Proceedings of the International Research Workshop on the Occurrence, Effects, and Fate of Microplastic Marine Debris, 9–11 September 2008, University of Washington Tacoma, Tacoma, WA, USA, NOAA Technical Memorandum NOS-OR&R-30, National Oceanic and Atmospheric Administration, Silver Spring, MD, USA, https://repository.library.noaa.gov/view/noaa/2509 (last access: 3 November 2026), 2009.

Athapaththu, A. M. A. I. K., Thushari, G. G. N., Dias, P. C. B., Abeygunawardena, A. P., Egodauyana, K. P. U. T., Liyanage, N. P. P., Pitawala, H. M. J. C., and Senevirathna, J. D. M.: Plastics in surface water of southern coastal belt of Sri Lanka (Northern Indian Ocean): Distribution and characterization by FTIR, Mar. Pollut. Bull., 161, 111750, https://doi.org/10.1016/j.marpolbul.2020.111750, 2020.

Auta, H. S., Emenike, C., and Fauziah, S.: Distribution and importance of microplastics in the marine environment: A review of the sources, fate, effects, and potential solutions, Environ. Int., 102, 165–176, https://doi.org/10.1016/j.envint.2017.02.013, 2017.

Azari, A., Ronsmans, S., Vanoirbeek, J. A. J., Hoet, P. H. M., and Ghosh, M.: Challenges in Raman spectroscopy of (micro)plastics: the interfering role of colourants, Environ. Pollut., 363, 125250, https://doi.org/10.1016/j.envpol.2024.125250, 2024.

Biswas, N. and Umapathy, S.: Structures, vibrational frequencies, and normal modes of substituted azo dyes: infrared, Raman, and density functional calculations, J. Phys. Chem. A, 104, 2734–2745, https://doi.org/10.1021/jp9929263, 2000.

Bond, T. C., Doherty, S. J., Fahey, D. W., Forster, P. M., Berntsen, T., DeAngelo, B. J., Flanner, M. G., Ghan, S., Kärcher, B., Koch, D., Kinne, S., Kondo, Y., Quinn, P. K., Sarofim, M. C., Schultz, M. G., Schulz, M., Venkataraman, C., Zhang, H., Zhang, S., Bellouin, N., Guttikunda, S. K., Hopke, P. K., Jacobson, M. Z., Kaiser, J. W., Klimont, Z., Lohmann, U., Schwarz, J. P., Shindell, D., Storelvmo, T., Warren, S. G., and Zender, C. S.: Bounding the role of black carbon in the climate system: A scientific assessment, J. Geophys. Res.-Atmos., 118, 5380–5552, https://doi.org/10.1002/jgrd.50171, 2013.

Boucher, J. and Friot, D.: Primary microplastics in the oceans: a global evaluation of sources, International Union for Conservation of Nature, Gland, Switzerland, 43 pp., https://doi.org/10.2305/IUCN.CH.2017.01.en, 2017.

Brahney, J., Mahowald, N., Prank, M., Cornwell, G., Klimont, Z., Matsui, H., and Prather, K. A.: Constraining the atmospheric limb of the plastic cycle, P. Natl. Acad. Sci. USA, 118, e2020719118, https://doi.org/10.1073/pnas.2020719118, 2021.

Budhavant, K., Andersson, A., Bosch, C., Kruså, M., Murthaza, A., Zahid, and Gustafsson, Ö.: Apportioned contributions of PM2.5 fine aerosol particles over the Maldives (northern Indian Ocean) from local sources vs long-range transport, Sci. Total Environ., 536, 72–78, https://doi.org/10.1016/j.scitotenv.2015.07.059, 2015.

Budhavant, K., Bikkina, S., Andersson, A., Asmi, E., Backman, J., Kesti, J., Zahid, H., Satheesh, S. K., and Gustafsson, Ö.: Anthropogenic fine aerosols dominate the wintertime regime over the northern Indian Ocean, Tellus B, 70, 1464871, https://doi.org/10.1080/16000889.2018.1464871, 2018.

Budhavant, K., Andersson, A., Holmstrand, H., Bikkina, P., Bikkina, S., Satheesh, S. K., and Gustafsson, Ö.: Enhanced Light-Absorption of Black Carbon in Rainwater Compared With Aerosols Over the Northern Indian Ocean, J. Geophys. Res.-Atmos., 125, e2019JD031246, https://doi.org/10.1029/2019JD031246, 2020.

Budhavant, K., Andersson, A., Holmstrand, H., Satheesh, S. K., and Gustafsson, Ö.: Black carbon aerosols over Indian Ocean

have unique source fingerprint and optical characteristics during monsoon season, P. Natl. Acad. Sci. USA, 120, e2210005120, https://doi.org/10.1073/pnas.2210005120, 2023.

Budhavant, K., Manoj, M. R., Nair, H. R. C. R., Gaita, S. M., Holmstrand, H., Salam, A., Muslim, A., Satheesh, S. K., and Gustafsson, Ö.: Changing optical properties of black carbon and brown carbon aerosols during long-range transport from the Indo-Gangetic Plain to the equatorial Indian Ocean, Atmos. Chem. Phys., 24, 11911–11925, https://doi.org/10.5194/acp-24-11911-2024, 2024.

Castro, M. A., Pereira, F. J., Aller, A. J., and Littlejohn, D.: Raman spectrometry as a screening tool for solvent-extracted azo dyes from polyester-based textile fibres, Polym. Test., 91, 106765, https://doi.org/10.1016/j.polymertesting.2020.106765, 2020.

Chen, Q., Shi, G., Revell, L. E., Zhang, J., Zuo, C., Wang, D., Le Ru, E. C., Wu, G., and Mitrano, D. M.: Long-range atmospheric transport of microplastics across the southern hemisphere, Nat. Commun., 14, 7898, https://doi.org/10.1038/s41467-023-43695-0, 2023.

Clarke, S., Holmstrand, H., Budhavant, K., Remani, M., Haslett, S., Rodiouchkina, K., Kooijman, E., and Gustafsson, Ö.: Isotopic apportionment of sulfate aerosols between natural and anthropogenic sources in the outflow of South Asia, Atmos. Chem. Phys., 26, 5333–5343, https://doi.org/10.5194/acp-26-5333-2026, 2026.

Connan, M., Perold, V., Dilley, B. J., Barbraud, C., Cherel, Y., and Ryan, P. G.: The Indian Ocean "garbage patch": Empirical evidence from floating macro-litter, Mar. Pollut. Bull., 169, 112559, https://doi.org/10.1016/j.marpolbul.2021.112559, 2021.

Corrigan, C. E., Ramanathan, V., and Schauer, J. J.: Impact of monsoon transitions on the physical and optical properties of aerosols, J. Geophys. Res.-Atmos., 111, D18208, https://doi.org/10.1029/2005JD006370, 2006.

Dasari, S., Andersson, A., Kim, S.-W., Holmstrand, H., Budhavant, K., and Gustafsson, Ö.: Observationally Constrained Wintertime Emission Fluxes and Atmospheric Lifetime of Black Carbon in South Asia, Environ. Sci. Tech. Let., 12, 710–717, https://doi.org/10.1021/acs.estlett.5c00079, 2025.

Donaldson, K. and Tran, C. L.: Inflammation caused by particles and fibres, Inhal. Toxicol., 14, 5–27, https://doi.org/10.1080/08958370175333613, 2002.

Dong, M., Zhang, Q., Xing, X., Chen, W., She, Z., and Luo, Z.: Raman spectra and surface changes of microplastics weathered under natural environments, Sci. Total Environ., 739, 139990, https://doi.org/10.1016/j.scitotenv.2020.139990, 2020.

Drinovec, L., Močnik, G., Zotter, P., Prévôt, A. S. H., Ruckstuhl, C., Coz, E., Rupakheti, M., Sciare, J., Müller, T., Wiedensohler, A., and Hansen, A. D. A.: The "dual-spot" Aethalometer: an improved measurement of aerosol black carbon with real-time loading compensation, Atmos. Meas. Tech., 8, 1965–1979, https://doi.org/10.5194/amt-8-1965-2015, 2015.

Dris, R., Gasperi, J., Mirande, C., Mandin, C., Guerrouache, M., Langlois, V., and Tassin, B.: A first overview of textile fibers, including microplastics, in indoor and outdoor environments, Environ. Pollut., 221, 453–458, https://doi.org/10.1016/j.envpol.2016.12.013, 2017.

Eberhard, T., Casillas, G., Zarus, G. M., and Barr, D. B.: Systematic review of microplastics and nanoplastics in indoor and outdoor air: identifying a framework and data needs for quantifying human inhalation exposures, J. Expo. Sci. Env. Epid., 34, 185–196, https://doi.org/10.1038/s41370-023-00634-x, 2024.

European Commission: Commission Recommendation of 18 October 2011 on the definition of nanomaterial (2011/696/EU), Official Journal of the European Union, L 275, 38–40, https://data.europa.eu/eli/reco/2011/696/oj (last access: 3 November 2026), 2011.

Ferrero, L., Casati, M., Nobili, L., D'Angelo, L., Rovelli, G., Sangiorgi, G., Rizzi, C., Perrone, M. G., Sansonetti, A., Conti, C., Bolzacchini, E., Bernardi, E., and Vassura, I.: Chemically and size-resolved particulate matter dry deposition on stone and surrogate surfaces inside and outside the low emission zone of Milan: application of a newly developed "Deposition Box", Environ. Sci. Pollut. Res., 25, 9402–9415, https://doi.org/10.1007/s11356-018-1220-2, 2018.

Ferrero, L., Scibetta, L., Markuszewski, P., Mazurkiewicz, M., Drozdowska, V., Makuch, P., Jutrzenka-Trzebiatowska, P., Zaleska-Medynska, A., Andò, S., Saliu, F., Nilsson, E. D., and Bolzacchini, E.: Airborne and marine microplastics from an oceanographic survey at the Baltic Sea: An emerging role of air-sea interaction?, Sci. Total Environ., 824, 153709, https://doi.org/10.1016/j.scitotenv.2022.153709, 2022.

Ferrero, L., Losi, N., Rigler, M., Gregorič, A., Colombi, C., D'Angelo, L., Cuccia, E., Cefalì, A. M., Gini, I., Doldi, A., Cerri, S., Maroni, P., Cipriano, D., Markuszewski, P., and Bolzacchini, E.: Determining the Aethalometer multiple scattering enhancement factor C from the filter loading parameter, Sci. Total Environ., 917, 170221, https://doi.org/10.1016/j.scitotenv.2024.170221, 2024.

Furukawa, T., Sato, H., Kita, Y., Matsukawa, K., Yamaguchi, H., Ochiai, S., Siesler, H. W., and Ozaki, Y.: Molecular structure, crystallinity and morphology of polyethylene/polypropylene blends studied by Raman mapping, scanning electron microscopy, wide angle X-ray diffraction, and differential scanning calorimetry, Polym. J., 38, 1127–1136, https://doi.org/10.1295/polymj.pj2006056, 2006.

Ghosh, A., Mandal, A., Karmakar, J., Mazumdar, S., and Darbha, G. K.: A pilot investigation of PM10-bound atmospheric microplastics over a protected mangrove ecosystem: Role of land–sea breeze circulation in marine and terrestrial inputs, Sci. Total Environ., 1004, 180797, https://doi.org/10.1016/j.scitotenv.2025.180797, 2025.

Global Modeling and Assimilation Office: MERRA-2 tavg1_2d_aer_Nx: 2d, 1-hourly, time-averaged, single-level, assimilation, aerosol diagnostics, version 5.12.4, NASA Goddard Earth Sciences Data and Information Services Center [data set], https://doi.org/10.5067/KLICLTZ8EM9D, 2015.

Gonda, I. and Abd El Khalik, A. F.: On the calculation of aerodynamic diameters of fibers, Aerosol Sci. Tech., 4, 233–238, https://doi.org/10.1080/02786828508959051, 1985.

González-Pleiter, M., Edo, C., Aguilera, Á., Viúdez-Moreiras, D., Pulido-Reyes, G., González-Toril, E., Osuna, S., de Diego-Castilla, G., Leganés, F., Fernández-Piñas, F., and Rosal, R.: Occurrence and transport of microplastics sampled within and above the planetary boundary layer, Sci. Total Environ., 761, 143213, https://doi.org/10.1016/j.scitotenv.2020.143213, 2021.

Guo, X., Lin, Z., Wang, Y., He, Z., Wang, M., and Jin, G.: In-line monitoring the degradation of polypropylene under multiple

extrusions based on Raman spectroscopy, Polymers, 11, 1698, https://doi.org/10.3390/polym11101698, 2019.

Gustafsson, Ö., Kruså, M., Zencak, Z., Sheesley, R. J., Granat, L., Engström, E., Praveen, P. S., Rao, P. S. P., Leck, C., and Rodhe, H.: Brown Clouds over South Asia: Biomass or Fossil Fuel Combustion?, Science, 323, 495–498, https://doi.org/10.1126/science.1164857, 2009.

Gustafsson, Ö., Budhavant, K., Chimurkar, N., Clarke, S., Dreyfus, G., Gong, X., Klimont, Z., Klingmüller, K., Kim, S.-W., Lelieveld, J., Myhre, G., Nair, H. R. C. R., Peng, J., Ramanathan, V., Rana, A., Manoj, M. R., Satheesh, S. K., Venkataraman, C., and Zhang, Q.: Atmospheric black carbon in the climate system, Nat. Rev. Earth Environ., 7, 312–328, https://doi.org/10.1038/s43017-026-00773-3, 2026.

Hildebrandt, L., El Gareb, F., Zimmermann, T., Klein, O., Kerstan, A., Emeis, K.-C., and Pröfrock, D.: Spatial distribution of microplastics in the tropical Indian Ocean based on laser direct infrared imaging and microwave-assisted matrix digestion, Environ. Pollut., 307, 119547, https://doi.org/10.1016/j.envpol.2022.119547, 2022.

Imhof, H. K., Sigl, R., Brauer, E., Feyl, S., Giesemann, P., Klink, S., Leupolz, K., Löder, M. G. J., Löschel, L. A., Missun, J., Muszynski, S., Ramsperger, A. F. R. M., Schrank, I., Speck, S., Steibl, S., Trotter, B., Winter, I., and Laforsch, C.: Spatial and temporal variation of macro-, meso- and microplastic abundance on a remote coral island of the Maldives, Indian Ocean, Mar. Pollut. Bull., 116, 340–347, https://doi.org/10.1016/j.marpolbul.2017.01.010, 2017.

Isa, V., Saliu, F., Becchi, A., Spadaccino, G., Quinto, M., Veronelli, M., Lasagni, M., Galli, P., and Lavorano, S.: Impacts of microplastics on reef-building corals: Disentangling the contribution of the chain scission products released by weathering, Sci. Total Environ., 975, 179239, https://doi.org/10.1016/j.scitotenv.2025.179239, 2025.

Islam, M. R., Welker, J., Salam, A., and Stone, E. A.: Plastic Burning Impacts on Atmospheric Fine Particulate Matter at Urban and Rural Sites in the USA and Bangladesh, ACS Environ. Au., 2, 409–417, https://doi.org/10.1021/acsenvironau.1c00054, 2022.

Kannankai, M. P. and Devipriya, S. P.: Atmospheric microplastic deposition in a coastal city of India: The influence of a landfill source on monsoon winds, Sci. Total Environ., 908, 168235, https://doi.org/10.1016/j.scitotenv.2023.168235, 2024.

Kapmeier, F. and Gonçalves, P.: Wasted paradise? Policies for Small Island States to manage tourism-driven growth while controlling waste generation: the case of the Maldives, Syst. Dynam. Rev., 34, 172–221, https://doi.org/10.1002/sdr.1607, 2018.

Kaushik, A., Gupta, P., Kumar, A., Saha, M., Varghese, E., Shukla, G., Suresh, K., and Gunthe, S. S.: Identification and physicochemical characterization of microplastics in marine aerosols over the northeast Arabian Sea, Sci. Total Environ., 912, 168705, https://doi.org/10.1016/j.scitotenv.2023.168705, 2024.

Kaza, S., Yao, L., Bhada-Tata, P., and Van Woerden, F.: What a waste 2.0: a global snapshot of solid waste management to 2050, World Bank, Washington, DC, https://doi.org/10.1596/978-1-4648-1329-0, 2018.

Kováts, N., Hubai, K., Sainnokhoi, T.-A., Eck-Varanka, B., Hoffer, A., Tóth, Á., Kakasi, B., and Teke, G.: Ecotoxic emissions generated by illegal burning of household waste, Chemosphere, 298, 134263, https://doi.org/10.1016/j.chemosphere.2022.134263, 2022.

Lewis, E. R. and Schwartz, S. E.: Sea salt aerosol production: mechanisms, methods, measurements, and models – a critical review, Geophysical Monograph Series, 152, American Geophysical Union, Washington, DC, https://doi.org/10.1029/GM152, 2004.

Li, J., Gao, F., Zhang, D., Cao, W., and Zhao, C.: Zonal Distribution Characteristics of Microplastics in the Southern Indian Ocean and the Influence of Ocean Current, J. Mar. Sci. Eng, 10, 290, https://doi.org/10.3390/jmse10020290, 2022.

Liu, Q., Vanmol, K., Lycke, S., Van Erps, J., Vandenabeele, P., Thienpont, H., and Ottevaere, H.: SERS using two-photon polymerized nanostructures for mycotoxin detection, RSC Adv., 10, 14274–14282, https://doi.org/10.1039/d0ra01909g, 2020.

Markuszewski, P., Budhavant, K., Gustafsson, Ö., Jutrzenka-Trzebiatowska, P., Stawiarz, K., Śmiszek, M., Nilsson, E. D., and Haslett, S.: Airborne and marine microplastics and atmospheric context measurements at the Maldives Climate Observatory Hanimaadhoo and adjacent coastal waters, January–February 2023, Zenodo [data set], https://doi.org/10.5281/zenodo.22102519, 2026.

Milani, A.: Unpolarized and polarized Raman spectroscopy of Nylon-6 polymorphs: a quantum chemical approach, J. Phys. Chem. B, 119, 3868–3874, https://doi.org/10.1021/jp5125266, 2015.

Müller, T., Laborde, M., Kassell, G., and Wiedensohler, A.: Design and performance of a three-wavelength LED-based total scatter and backscatter integrating nephelometer, Atmos. Meas. Tech., 4, 1291–1303, https://doi.org/10.5194/amt-4-1291-2011, 2011.

Munshi, S., Banerjee, S., and Chakraborty, I.: Thilafushi a toxic bomb: learning from an island's solid-waste-management practice, International Journal of Architecture and Infrastructure Planning, 8, 1–12, https://doi.org/10.37628/jaip.v8i2.954, 2022.

Nair, H. R. C. R., Budhavant, K., Manoj, M. R., Andersson, A., Satheesh, S. K., Ramanathan, V., and Gustafsson, Ö.: Aerosol demasking enhances climate warming over South Asia, npj Clim. Atmos. Sci., 6, 39, https://doi.org/10.1038/s41612-023-00367-6, 2023.

O'Dowd, C. D. and de Leeuw, G.: Marine aerosol production: a review of the current knowledge, Philos. T. R. Soc. A, 365, 1753–1774, https://doi.org/10.1098/rsta.2007.2043, 2007.

Oehlschlägel, L. M., Schmid, S., Lehmann, M., Gekle, S., and Held, A.: Water–air transfer rates of microplastic particles through bubble bursting as a function of particle size, Microplastics and Nanoplastics, 4, 1, https://doi.org/10.1186/s43591-023-00079-x, 2024.

Patti, T. B., Fobert, E. K., Reeves, S. E., and Burke da Silva, K.: Spatial distribution of microplastics around an inhabited coral island in the Maldives, Indian Ocean, Sci. Total Environ., 748, 141263, https://doi.org/10.1016/j.scitotenv.2020.141263, 2020.

Pattiaratchi, C., van der Mheen, M., Schlundt, C., Narayanaswamy, B. E., Sura, A., Hajbane, S., White, R., Kumar, N., Fernandes, M., and Wijeratne, S.: Plastics in the Indian Ocean – sources, transport, distribution, and impacts, Ocean Sci., 18, 1–28, https://doi.org/10.5194/os-18-1-2022, 2022.

Peñalver, R., Zapata, F., Arroyo-Manzanares, N., López-García, I., and Viñas, P.: Raman spectroscopic strategy for the discrimination of recycled polyethylene terephtha-

late in water bottles, J. Raman Spectrosc., 54, 107–112, https://doi.org/10.1002/jrs.6457, 2023.

Perera, K., Ziajahromi, S., Bengtson Nash, S., Manage, P. M., and Leusch, F. D. L.: Airborne Microplastics in Indoor and Outdoor Environments of a Developing Country in South Asia: Abundance, Distribution, Morphology, and Possible Sources, Environ. Sci. Technol., 56, 16676–16685, https://doi.org/10.1021/acs.est.2c05885, 2022.

Perraki, M., Skliros, V., Mecaj, P., Vasileiou, E., Salmas, C., Papanikolaou, I., and Stamatis, G.: Identification of Microplastics Using μ-Raman Spectroscopy in Surface and Groundwater Bodies of SE Attica, Greece, Water, 16, 843, https://doi.org/10.3390/w16060843, 2024.

Petzold, A., Ogren, J. A., Fiebig, M., Laj, P., Li, S.-M., Baltensperger, U., Holzer-Popp, T., Kinne, S., Pappalardo, G., Sugimoto, N., Wehrli, C., Wiedensohler, A., and Zhang, X.-Y.: Recommendations for reporting "black carbon" measurements, Atmos. Chem. Phys., 13, 8365–8379, https://doi.org/10.5194/acp-13-8365-2013, 2013.

Prata, J. C., Padrão, J., Khan, M. T., and Walker, T. R.: Do's and don'ts of microplastic research: a comprehensive guide, Water Emerging Contaminants & Nanoplastics, 3, 8, https://doi.org/10.20517/wecn.2023.61, 2024.

Raguso, C., Saliu, F., Lasagni, M., Galli, P., Clemenza, M., and Montano, S.: First detection of microplastics in reef-building corals from a Maldivian atoll, Mar. Pollut. Bull., 180, 113773, https://doi.org/10.1016/j.marpolbul.2022.113773, 2022.

Ramachandran, S. and Rupakheti, M.: Inter-annual and seasonal variations in columnar aerosol characteristics and radiative effects over the Pokhara Valley in the Himalayan foothills – Composition, radiative forcing, and atmospheric heating, Environ. Pollut., 264, 114799, https://doi.org/10.1016/j.envpol.2020.114799, 2020.

Ramana, M. V. and Ramanathan, V.: Abrupt transition from natural to anthropogenic aerosol radiative forcing: Observations at the ABC-Maldives Climate Observatory, J. Geophys. Res.-Atmos., 111, D20207, https://doi.org/10.1029/2006JD007063, 2006.

Ramanathan, V. and Carmichael, G.: Global and regional climate changes due to black carbon, Nat. Geosci., 1, 221–227, https://doi.org/10.1038/ngeo156, 2008.

Ramanathan, V., Crutzen, P. J., Lelieveld, J., Mitra, A. P., Althausen, D., Anderson, J., Andreae, M. O., Cantrell, W., Cass, G. R., Chung, C. E., Clarke, A. D., Coakley, J. A., Collins, W. D., Conant, W. C., Dulac, F., Heintzenberg, J., Heymsfield, A. J., Holben, B., Howell, S., Hudson, J., Jayaraman, A., Kiehl, J. T., Krishnamurti, T. N., Lubin, D., McFarquhar, G., Novakov, T., Ogren, J. A., Podgorny, I. A., Prather, K., Priestley, K., Prospero, J. M., Quinn, P. K., Rajeev, K., Rasch, P., Rupert, S., Sadourny, R., Satheesh, S. K., Shaw, G. E., Sheridan, P., and Valero, F. P. J.: Indian Ocean Experiment: An integrated analysis of the climate forcing and effects of the great Indo-Asian haze, J. Geophys. Res.-Atmos., 106, 28371–28398, https://doi.org/10.1029/2001JD900133, 2001.

Rao, M. N., Ghude, S. D., Nivdange, S. D., Panchang, R., Pipal, A. S., Mukherjee, A., Sharma, H., and Kumar, V.: Characterization and health risk assessment of airborne microplastics in Delhi NCR, Sci. Rep., 15, 25662, https://doi.org/10.1038/s41598-025-04306-8, 2025.

Rifa, T. and Hossain, M. B.: Micro Plastic Pollution in South Asia: The Impact of Plastic Pollution over the Unsustainable Development Goals, Lex Publica, 9, 1–28, https://doi.org/10.58829/lp.9.2.2022.01-28, 2022.

Royle, J., Jack, B., Parris, H., Elliott, T., Castillo, A. C., Kalawana, S., Nashfa, H., and Woodall, L. C.: Plastic Drawdown: A rapid assessment tool for developing national responses to plastic pollution when data availability is limited, as demonstrated in the Maldives, Global Environ. Chang., 72, 102442, https://doi.org/10.1016/j.gloenvcha.2021.102442, 2022.

Rytelewska, S. and Dąbrowska, A.: The Raman spectroscopy approach to different freshwater microplastics and quantitative characterization of polyethylene aged in the environment, Microplastics, 1, 263–281, https://doi.org/10.3390/microplastics1020019, 2022.

Saliu, F., Montano, S., Garavaglia, M. G., Lasagni, M., Seveso, D., and Galli, P.: Microplastic and charred microplastic in the Faafu Atoll, Maldives, Mar. Pollut. Bull., 136, 464–471, https://doi.org/10.1016/j.marpolbul.2018.09.023, 2018.

Saliu, F., Montano, S., Leoni, B., Lasagni, M., and Galli, P.: Microplastics as a threat to coral reef environments: Detection of phthalate esters in neuston and scleractinian corals from the Faafu Atoll, Maldives, Mar. Pollut. Bull., 142, 234–241, https://doi.org/10.1016/j.marpolbul.2019.03.043, 2019.

Schlitzer, R.: Ocean Data View, https://odv.awi.de (last access: 24 July 2026), 2025.

Sheesley, R. J., Kirillova, E., Andersson, A., Kruså, M., Praveen, P. S., Budhavant, K., Safai, P. D., Rao, P. S. P., and Gustafsson, Ö.: Year-round radiocarbon-based source apportionment of carbonaceous aerosols at two background sites in South Asia, J. Geophys. Res.-Atmos., 117, D10202, https://doi.org/10.1029/2011JD017161, 2012.

Spencer, M. T., Holecek, J. C., Corrigan, C. E., Ramanathan, V., and Prather, K. A.: Size-resolved chemical composition of aerosol particles during a monsoonal transition period over the Indian Ocean, J. Geophys. Res.-Atmos., 113, D16305, https://doi.org/10.1029/2007JD008657, 2008.

Stegelius, K., Thompson, P., Karbiener, P., Markuszewski, P., Prevot, A. S. H., Tripathi, S. N., Mohr, C., Heikkinen, L., Budhavant, K., and Haslett, S. L.: Aerosol processing during long-range transport governs the chemical composition of haze over the northern Indian Ocean, EGUsphere [preprint], https://doi.org/10.5194/egusphere-2026-914, 2026.

Stevens, G. M. W. and Froman, N.: The Maldives Archipelago, in: World Seas: an Environmental Evaluation, 2nd Edn., edited by: Sheppard, C., Academic Press, 211–236, https://doi.org/10.1016/B978-0-08-100853-9.00010-5, 2019.

Szymańska-Chargot, M., Cybulska, J., and Zdunek, A.: Sensing the structural differences in cellulose from apple and bacterial cell wall materials by Raman and FT-IR spectroscopy, Sensors, 11, 5543–5560, https://doi.org/10.3390/s110605543, 2011.

Tauhiduzzaman, M., Salsabil, N., Khatun, K., Muhaiminul Haque, M., Habib, A., Shamima Akter, M., Islam, S., Hasibuzzaman, M., Rahman, I. M., Ahmmed, M., Zaman, S., Chakraborty, T. K., and Ghosh, G. C.: Atmospheric microplastics deposition in Dhaka City, Bangladesh: occurrence, distribution and ecological risk assessment, Atmos. Pollut. Res., 17, 102856, https://doi.org/10.1016/j.apr.2025.102856, 2025.

Trainic, M., Flores, J. M., Pinkas, I., Pedrotti, M. L., Lombard, F., Bourdin, G., Gorsky, G., Boss, E., Rudich, Y., Vardi, A., and Koren, I.: Airborne microplastic particles detected in the remote marine atmosphere, Commun. Earth Environ., 1, 64, https://doi.org/10.1038/s43247-020-00061-y, 2020.

Turner, A.: Paint particles in the marine environment: An overlooked component of microplastics, Water Res. X, 12, 100110, https://doi.org/10.1016/j.wroa.2021.100110, 2021.

van der Does, M., Knippertz, P., Zschenderlein, P., Harrison, R. G., and Stuut, J.-B. W.: The mysterious long-range transport of giant mineral dust particles, Sci. Adv., 4, eaau2768, https://doi.org/10.1126/sciadv.aau2768, 2018.

Vasse, G. F. and Melgert, B. N.: Microplastic and plastic pollution: impact on respiratory disease and health, European Respiratory Review, 33, 230226, https://doi.org/10.1183/16000617.0226-2023, 2024.

Wang, X., Li, C., Liu, K., Zhu, L., Song, Z., and Li, D.: Atmospheric microplastic over the South China Sea and East Indian Ocean: abundance, distribution and source, J. Hazard. Mater., 389, 121846, https://doi.org/10.1016/j.jhazmat.2019.121846, 2020.

Wang, Z., Hu, M., Fan, J., Zheng, H., Wang, C., Ahmad, M., Li, L., Zhao, G., Zhang, G., Zhang, Y., Hu, J., and Wang, Y.: Microplastic pollution in the Indian Ocean: Fiber-dominated contamination and comparative bioaccumulation in Auxis thazard and Symplectoteuthis oualaniensis, Mar. Environ. Res., 210, 107304, https://doi.org/10.1016/j.marenvres.2025.107304, 2025.

Zeng, E. Y. (Ed.): Microplastic contamination in aquatic environments: an emerging matter of environmental urgency, Elsevier, Amsterdam, the Netherlands, https://doi.org/10.1016/C2022-0-00176-8, 2023.

Zhou, L., Li, J., Zhao, C., Yin, J., Ding, J., Cao, W., and Fan, W.: Overview of monitoring methods and environmental distribution: Microplastics in the Indian Ocean, Mar. Pollut. Bull., 214, 117715, https://doi.org/10.1016/j.marpolbul.2025.117715, 2025.